

# Radio imaging of the Subaru/XMM-Newton Deep Field - I. The $100\mu\text{Jy}$ catalogue, optical identifications, and the nature of the faint radio source population

Chris Simpson<sup>1,2\*</sup>, Alejo Martínez-Sansigre<sup>3</sup>, Steve Rawlings<sup>3</sup>, Rob Ivison<sup>4,5</sup>, Masayuki Akiyama<sup>6</sup>, Kazuhiro Sekiguchi<sup>6</sup>, Tadafumi Takata<sup>7</sup>, Yoshihiro Ueda<sup>8</sup>, and Mike Watson<sup>9</sup>

<sup>1</sup>*Astrophysics Research Institute, Liverpool John Moores University, Twelve Quays House, Egerton Wharf, Birkenhead CH41 1LD*

<sup>2</sup>*Department of Physics, University of Durham, South Road, Durham DH1 3LE*

<sup>3</sup>*Department of Physics, University of Oxford, Denys Wilkinson Building, Keble Road, Oxford OX1 3RH*

<sup>4</sup>*UK Astronomy Technology Centre, Royal Observatory, Blackford Hill, Edinburgh EH9 3HJ*

<sup>5</sup>*Institute for Astronomy, University of Edinburgh, Royal Observatory, Blackford Hill, Edinburgh EH9 3HJ*

<sup>6</sup>*Subaru Telescope, National Astronomical Observatory of Japan, 650 N. A'ohōkū Place, Hilo, HI 96720, USA*

<sup>7</sup>*National Astronomical Observatory of Japan, Mitaka, Tokyo 181-8588, Japan*

<sup>8</sup>*Department of Astronomy, Kyoto University, Kyoto 606-8502, Japan*

<sup>9</sup>*Department of Physics and Astronomy, University of Leicester, Leicester LE1 7RH*

Version of 17 October 2018

## ABSTRACT

We describe deep radio imaging at 1.4 GHz of the 1.3 square degree Subaru/XMM-Newton Deep Field (SXDF), made with the Very Large Array in B and C configurations. We present a radio map of the entire field, and a catalogue of 505 sources covering 0.8 square degrees to a peak flux density limit of  $100\mu\text{Jy}$ . Robust optical identifications are provided for 90 per cent of the sources, and suggested IDs are presented for all but 14 (of which 7 are optically blank, and 7 are close to bright contaminating objects). We show that the optical properties of the radio sources do not change with flux density, suggesting that AGNs continue to contribute significantly at faint flux densities. We test this assertion by cross-correlating our radio catalogue with the X-ray source catalogue and conclude that radio-quiet AGNs become a significant population at flux densities below  $300\mu\text{Jy}$ , and may dominate the population responsible for the flattening of the radio source counts if a significant fraction of them are Compton-thick.

**Key words:** catalogues — galaxies: active — radio continuum: galaxies — surveys

## 1 INTRODUCTION

Surveys of extragalactic radio sources find two broad populations of object: active galactic nuclei (AGNs), and star-forming galaxies. The two processes which power these objects (accretion onto supermassive black holes, and star formation) are believed to be intimately linked by a mechanism or mechanisms collectively known as ‘AGN-driven feedback’ (e.g., Croton et al. 2006; Bower et al. 2006) which produces the observed tight correlation between the masses of the central black hole and the stellar bulge (e.g., Ferrarese & Merritt 2000; Gebhardt et al. 2000). Radio surveys therefore provide the opportunity to study the cosmic evolution of both these important processes.

Spectroscopically-complete samples of radio sources exist at equivalent 1.4-GHz flux densities of  $\sim 100\text{mJy}$  (e.g., Willott et al. 2002), and these samples are dominated by objects with pow-

erful radio-emitting jets which carry a kinetic power comparable to their optical/X-ray photoionizing luminosity (e.g., Rawlings & Saunders 1991). These objects are commonly referred to as ‘radio-loud’ AGNs, and have radio luminosities and morphologies which place them above the Fanaroff & Riley (1974) break ( $L_{178\text{MHz}} \sim 2 \times 10^{25} \text{W Hz}^{-1} \text{sr}^{-1}$ ) and they are classified as FR Class II objects. At increasingly fainter flux densities, the observed source counts follow a power-law to  $\sim 1\text{mJy}$  (e.g., Windhorst et al. 1993) and the spectroscopic completeness of samples selected at these flux density limits decreases, in part because an increasing fraction of the objects have spectra which show little sign of optical nuclear activity (e.g., Waddington et al. 2001), apparently because their supermassive black holes are accreting at a much lower rate. While these are still genuine radio-loud AGNs due to their ratio of optical and radio energy outputs, the radio luminosities place them below the Fanaroff–Riley break as FR I sources.

The cosmic evolution of these two classes of radio-loud AGNs appears to differ. While it has been known for many years that the

\* E-mail: cjs@astro.livjm.ac.uk

population of the most powerful (FR II) extragalactic radio sources undergoes very strong positive evolution (e.g., Dunlop & Peacock 1990), the less powerful (FR I) sources evolve less strongly, possibly with a constant comoving space density (e.g., Clewley & Jarvis 2004). By modelling the evolution of the radio luminosity functions for these sources, it can be shown that their contribution to the total radio source counts should continue as a power law to even fainter flux densities (e.g., Jarvis & Rawlings 2004). However, below 1 mJy the observed counts flatten (when normalized to Euclidean), and this is attributed to the appearance of a new population of radio sources which do not contribute significantly at higher flux densities, but which start to dominate at  $S_{1.4} \lesssim 300 \mu\text{Jy}$ . This new population is usually believed to be star-forming galaxies (Condon 1984; Windhorst et al. 1985), and the faint source counts have been successfully modelled on the basis of this interpretation (e.g., Seymour et al. 2004). Recently, however, Jarvis & Rawlings (2004) have suggested that the source counts may flatten due to the ‘radio-quiet’ AGN population, by which we mean supermassive black holes with a high accretion rate but a low ratio of radio to optical/X-ray luminosity. For quasars, where the non-stellar optical radiation is seen directly, the distinction between radio-loud and radio-quiet can also be made on the basis of the ratio of radio to optical fluxes (e.g., Kellermann et al. 1989). Since radio-quiet AGNs are known to be far more prevalent than their radio-loud counterparts, this population could indeed be important.

The fact that we still do not know the nature of the population(s) which dominate at flux densities  $\lesssim 300 \mu\text{Jy}$  can be attributed to two factors. First, most of the effort to follow up radio source samples spectroscopically to high completeness has been devoted to samples selected at either bright ( $\gtrsim 100 \text{ mJy}$ ; e.g., Willott et al. 2002) or very faint flux densities ( $\lesssim 50 \mu\text{Jy}$ ) from multi-wavelength studies of deep (and hence small-area) fields (e.g., Richards et al. 1998). As a result, there has been very little study of the sources in the range  $100 \mu\text{Jy} \lesssim S_{1.4} \lesssim 500 \mu\text{Jy}$ , where the new population(s) begin to appear. Even when studies have focused on this flux density range (e.g., Hopkins et al. 2003), the optical counterparts span such a large range in apparent magnitude that it is difficult to obtain IDs and subsequent photometry and spectroscopy of all members of a sample. Results have therefore been equivocal and even contradictory. Windhorst et al. (1985) identified such sources with faint blue galaxies whose colours suggested that they were undergoing significant star formation. Spectroscopy by Benn et al. (1993) supported this interpretation, but later work by Grupponi, Mignoli & Zamorani (1999) indicated that early-type galaxies were the dominant population. They attributed this difference to their deeper limit for optical identifications.

The key to solving this issue is therefore to increase the identification fraction of faint radio surveys as close to 100 per cent as possible by combining deep multi-colour imaging and moderate resolution (a few arcseconds, so as not to resolve out galactic-scale starbursts and hence bias a sample in favour of active galaxies) radio mapping over a degree-size field, so that there will be a statistically useful number of such objects. The Subaru/*XMM-Newton* Deep Field (SXDF; Sekiguchi et al. 2001, 2006) is ideal for this task, as it is home to extremely deep optical and near-infrared imaging (Furusawa et al. 2006; Lawrence et al. 2006). Deep (50–100 ksec) X-ray exposures with *XMM-Newton* (Ueda et al. 2006) have also been made in the SXDF, enabling the active galactic nucleus (AGN) content of the radio source population to be studied. We have therefore undertaken deep radio observations of this field to enable the  $\sim 100 \mu\text{Jy}$  radio source population to be identified

**Table 1.** Locations of the 14 field centres for the VLA observations.

Pointing	RA	dec	rms noise
	(J2000.0)		( $\mu\text{Jy}$ )
1	02 18 30	−05 04 20	20
2	02 18 30	−05 30 20	20
3	02 17 30	−05 04 20	21
4	02 17 00	−05 17 20	20
5	02 19 00	−04 51 20	21
6	02 18 00	−04 51 20	21
7	02 19 30	−05 04 20	20
8	02 18 00	−05 17 20	21
9	02 17 00	−04 51 20	21
10	02 18 30	−04 38 20	20
11	02 17 30	−04 38 20	22
12	02 16 30	−05 04 20	22
13	02 17 30	−05 30 20	20
14	02 19 00	−05 17 20	27

and studied with greater completeness than has previously been possible.

The format of this paper is as follows. In Section 2 we describe the radio observations and reduction methods, and in Section 3 we explain how we have determined and corrected for incompleteness in the catalogue. In Section 4 we describe how optical identifications were made, and report on our analysis of the faint radio source population. In Section 5 we summarize our main results. Radio maps of sources which are either significantly extended or have an uncertain optical identification are presented in an Appendix. All magnitudes quoted in this paper are calibrated on the AB scale.

## 2 OBSERVATIONS AND REDUCTION

The SXDF was observed with the National Radio Astronomy Observatory’s Very Large Array (VLA) in B-array using the 14 overlapping pointings arranged in a hexagonal pattern listed in Table 1. Three test observations of pointings 1, 4 and 6 were taken on 2001 May 17, and the rest of the data were obtained in 13 runs, each lasting 4.5 hours, between 2002 August 10 and September 9. Each of these runs consisted of 5 snapshots of about 45-minutes duration separated by phase and bandpass calibration observations of VLA calibrators 0217+017 and 0241−082 and a single visit to the primary calibrator 3C 48 (0137+331). All data were taken in the ‘4 IF’ spectral line mode with central frequencies set at 1.3649 and 1.4351 GHz, each with seven useable channels of width 3.125 MHz per IF. The correlator delivered both ‘LL’ and ‘RR’ correlated signals from the left (‘L’) and right (‘R’) circular polarizations from each antenna, and a 5-second averaging time was used. The maximum loss of amplitude (for objects 15 arcmin away from the field centres) caused by the finite bandwidth and averaging time is calculated to be 0.9% and 0.02%, respectively, and can be considered negligible.

All 14 pointings were re-observed in C-array on 2003 January 15 to provide additional information on larger angular scales. Apart from the array configuration, the set-up for these observations was identical to that for the B-array observations and total integration times for each pointing were around 5 minutes.

The summer 2002 B-array observations were severely affected by narrow-band interference signals and much manual flagging of these datasets were required. After such editing, and standard phase

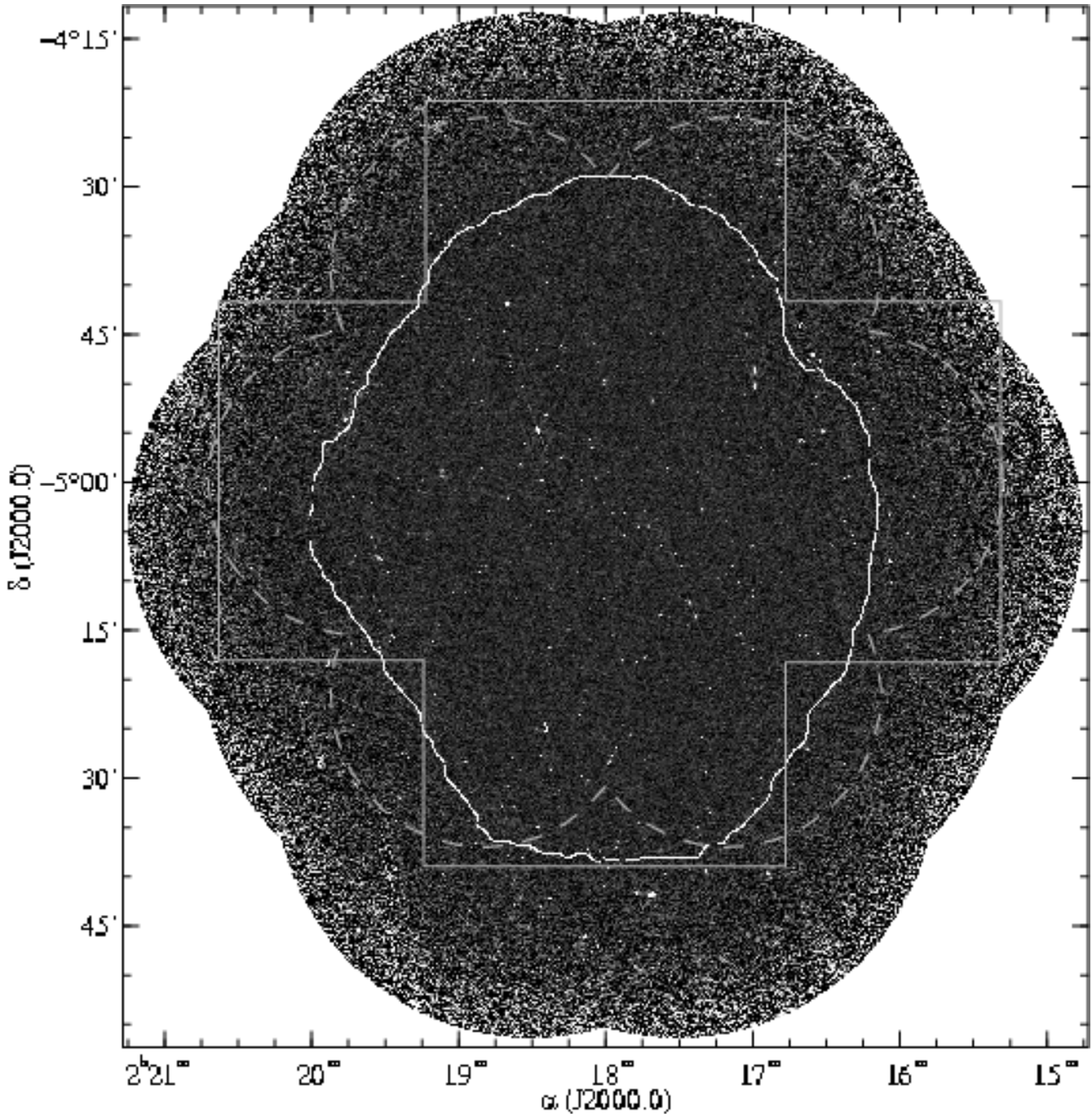


**Figure 1.** Final radio mosaic of the SXDF. The solid gray line shows the region covered by the ultra-deep Suprime-Cam images (Furusawa et al. 2006), while the dashed gray line shows the area observed with the seven *XMM-Newton* pointings (Ueda et al. 2006). The solid white line indicates the region where the rms noise is less than  $20 \mu\text{Jy beam}^{-1}$ , from which the  $100 \mu\text{Jy}$  catalogue described here has been constructed. Some mapping artefacts are still evident.

and flux density calibrations, data in each array and pointing positions were processed using the *AIPS* task *IMAGR*. The CLEAN algorithm within *IMAGR* worked on a continuous area of radius 0.52 degrees alongside smaller fields centred on known NVSS sources (implemented using the *AIPS* task *SETFC*). The central region of each pointing was divided into 13 facets which were eventually combined with the *AIPS* task *FLATN*. Maps made from the B-array data were self-calibrated for phase (using the *AIPS* task *CALIB*) and then re-mapped with *IMAGR*: the clean component model of the sky was also used to self-calibrate the C-array data be-

fore the B- and C-array UV data were combined using the *AIPS* task *DBCON*. Multiple cycles of running *IMAGR* and then applying self-calibration techniques, initially on phase and finally on phase and amplitude, were needed to improve the dynamic range of each image. Various antennas with time-dependent problems were also identified during this process and corrupted UV data were excised. A consistent rms noise  $\sim 20\text{--}22 \mu\text{Jy}$  was achieved in 13 of the 14 separately processed pointings, with an anomalously high noise level  $\sim 27 \mu\text{Jy}$  in the pointing centred at 021900–051720; the dynamic range of this pointing could not be improved despite exten-

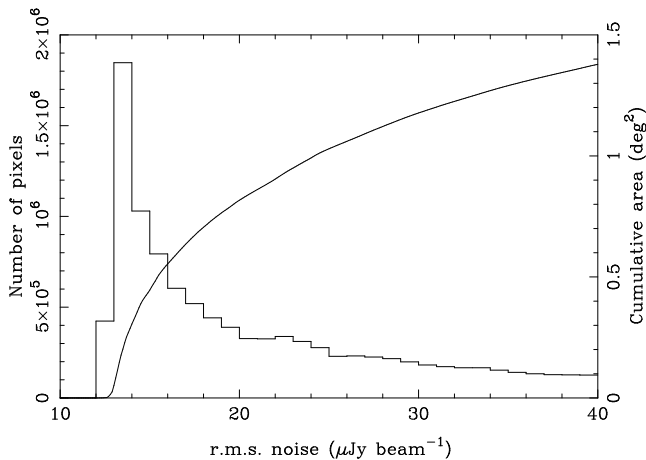


**Figure 2.** Distribution of pixel values (each pixel is  $1.25''$  square) in the noise map, as determined by SExtractor from interpolation between the centres of the meshes. The cumulative area covered by pixels with noise below a given value is shown by the smooth curve.

sive effort. Finally, the 14 pointings were combined with FLATN to provide a final map in which the primary beam correction was consistently applied. This final image still has mapping artefacts around the brightest sources, some of which might conceivably be removable by more careful, manually intensive applications of the CLEAN algorithm. The synthesized beam varies slightly across the image but has a roughly elliptical shape characterized by  $\sim 5'' \times 4''$  at PA  $\approx 170^\circ$ . We present the final mosaic, and show its relationship to the areas covered by the optical and X-ray data, in Fig. 1.

We calculate the rms noise as a function of position in our final mosaic using the SExtractor software package (Bertin & Arnouts 1996). A mesh size of  $64 \times 64$  pixels, corresponding to 80 arcseconds on a side, was used to compute the local background, and the results are presented in Fig. 2.

### 3 SOURCE COUNTS

For the remainder of this paper, we concentrate only on the region where the rms noise per pixel, as determined from the SExtractor mesh, is less than  $20 \mu\text{Jy beam}^{-1}$ . This region covers 0.808 square degrees (Figs 1 and 2) and is well-matched to the area covered by the ultra-deep Suprime-Cam images of this region (Furusawa et al. 2006).

#### 3.1 Source extraction

The *AIPS* task SAD was used to find and extract all the sources with a peak flux density  $\geq 100 \mu\text{Jy}$ , corresponding to signal-to-noise ratios of between five and eight. A conservative cut was chosen to minimize the appearance of spurious sources. The positions from the SAD catalogue were used to create the final SXDF radio catalogue as described below.

Since SAD works by fitting and then subtracting Gaussians to the radio image, it is liable to two sources of error. First, it systematically underestimates the flux of extended sources which contain diffuse emission. Sources which were clearly extended were dealt with by first defining masks to exclude them from the SAD catalogue, and then using the *AIPS* task TVSTAT to measure their flux densities. It was possible to do this on an object-by-object basis due to their small number (14); examples include

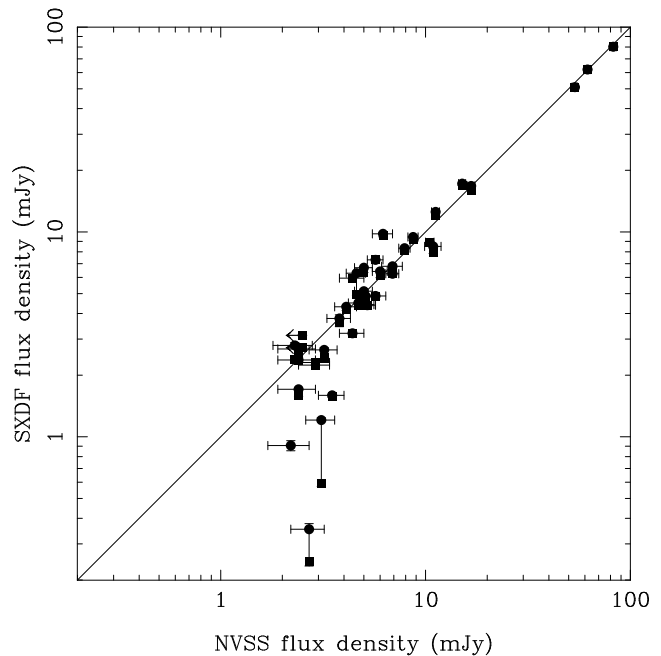


**Figure 3.** Comparison of our flux densities with those from the NVSS catalogue (Condon et al. 1998). All but one of the NVSS sources can be associated with a source in our catalogue, and we plot these as squares. We have also investigated the effect of confusion caused by the large beam of the NVSS, by including the flux from nearby sources in our catalogue (weighted by a Gaussian with FWHM =  $45''$ ), and we plot these measurements as circles (the NVSS source not uniquely identified with a source in our catalogue appears to be due to the confused flux from a number of faint sources). The solid line indicates an equality of flux densities.

VLA J021724–05218 and VLA J021827–04546. To investigate possible biases in the flux density measurements of the brightest radio sources, we compared our measurements with those of the NVSS (Condon et al. 1998), and we find no systematic effects except for those NVSS sources at the survey flux limit (Fig. 3).

Secondly, as discussed in detail by Condon (1997), Gaussian fitting routines such as SAD tend to systematically underestimate the angular sizes and overestimate the peak flux densities when there is noise present. We have attempted to produce an algorithm which derives unbiased flux density estimates for all sources. First, every source in the SAD catalogue had its flux density measured in a series of concentric circular apertures of diameter 7.5, 10, 12.5, ..., 35 arcseconds, as well as by the IMFIT task. The flux densities in the 12.5 and 35-arcsecond apertures and the IMFIT measurement were compared for each source, and if any pair of these measurements disagreed by more than  $2\sigma$ , the source was flagged as possibly confused, and a flux density was measured by hand using the TVSTAT task.

The following procedure was used to determine the 1.4-GHz flux densities of the remaining sources. Each source in the SAD catalogue has a peak flux density  $S_{\text{peak}}$  and FWHM measurements along the major and minor axes,  $\theta_M$  and  $\theta_m$ , respectively. Uncertainties,  $\sigma_M$  and  $\sigma_m$  can be assigned to these measurements, following Condon (1997) and Condon et al. (1998). These angular sizes are compared to the size of the CLEAN beam,  $\theta_M^* \times \theta_m^*$ . A source was considered to be unresolved if

$$\left[ \max \left( 0, \frac{\theta_M - \theta_M^*}{\sigma_M} \right) \right]^2 + \left[ \max \left( 0, \frac{\theta_m - \theta_m^*}{\sigma_m} \right) \right]^2 \leq 2^2,$$

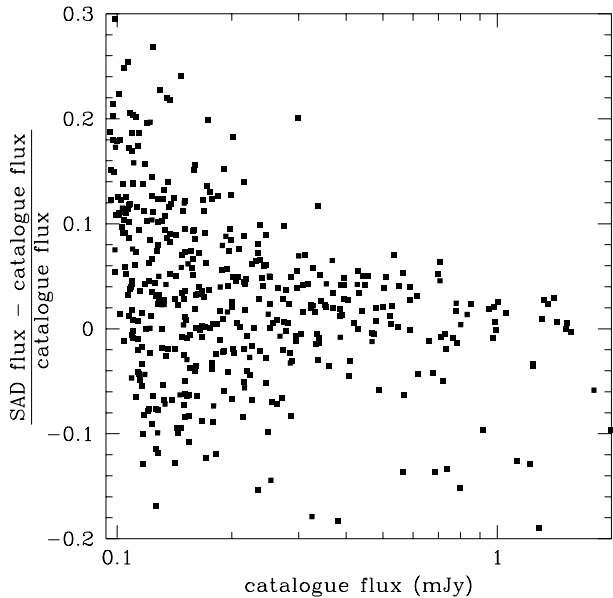


**Figure 4.** Relationship between the source flux densities as determined by the *AIPS* task *SAD* and the flux densities used in the catalogue, demonstrating the bias in the task. Sources significantly below the main locus of points are extended.

in which case it was assigned a flux density of

$$S_{\text{unres}} = S_{\text{peak}} \left( \frac{\theta_M \theta_m}{\theta_M^* \theta_m^*} \right)^{1/2}$$

(Condon 1997; Condon et al. 1998), with an appropriately calculated uncertainty  $\sigma_{\text{unres}}$ . Due to the tendency of *SAD* to overestimate flux densities, 17 sources in the original catalogue were found to be unresolved but have flux densities  $S < 100 \mu\text{Jy}$ . These sources were not included in the final catalogue.

Additionally, an aperture flux density,  $S_{\text{ap}}$ , was assigned to each source using the concentric aperture measurements: working outwards from the smallest aperture, when the measurements in two consecutive annuli were both consistent (at the  $1\sigma$  level) with zero, the flux density measured within the boundary between these annuli was assigned. Sources with  $S_{\text{ap}} \geq S_{\text{unres}} + 2\sigma_{\text{unres}}$  were inspected by eye and the aperture flux was used in the catalogue unless the difference was due to confusion. This method should ensure that sources with strong unresolved cores and fainter extended emissions do not have their flux densities systematically underestimated. The aperture flux was also used for all sources which were not considered to be unresolved by the above criterion. We demonstrate in Fig. 4 the systematic difference between our catalogue fluxes and the biased *SAD* fluxes.

In a number of cases, widely-separated multiple components of a single source were found by the detection algorithm. These instances were identified by overlaying the radio contours on a true-colour optical image of the field. In this manner, it became easy to distinguish FR II double radio sources (where there was no optical counterpart at the location of either radio-emitting component, but there was a plausible ID – usually a red galaxy – between them) from instances where distinct (but possibly physically related) sources of similar radio flux density had a small angular separation. More detail on the optical identification will be given in Section 4, but we note that a method independent of the opti-

cal data, such as that suggested by Bondi et al. (2003), would not work for our catalogue, as it would both fail to identify large double sources, and also incorrectly associate distinct sources having small angular separations. In total, there are 505 unique sources in the final catalogue.

### 3.2 Completeness

Two issues need to be considered when interpreting the measured source count distribution. First is the well-known effect of Eddington bias (Eddington 1913), where random measurement errors result in more objects being boosted into a given bin of flux density from the one below than are removed from that bin by having a measured flux density lower than the value (provided the source counts have the correct sign of slope). This effect can be modelled since the observed source counts,  $N'(S)$ , are a function of the true source counts,  $N(S)$ , and the distribution of pixel values in the noise map. If  $\sigma$  is the rms noise of a pixel and  $f(\sigma) d\sigma$  is the fraction of pixels in the noise map with values between  $\sigma$  and  $\sigma + d\sigma$ , then

$$N'(S) = \int_0^\infty \int_{-\infty}^\infty \frac{1}{\sqrt{2\pi}} e^{-\zeta^2/2} N(S + \zeta\sigma) f(\sigma) d\zeta d\sigma. \quad (1)$$

This equation cannot be inverted, but we can use a range of plausible functional forms for  $N(S)$  to examine the amount by which source counts will be overestimated due to Eddington bias, i.e.,  $N'(S)/N(S)$ .

The second effect is the incompleteness to extended sources, since a source only appears in our catalogue if its peak flux density is greater than our threshold of  $100 \mu\text{Jy beam}^{-1}$ . To account for this requires knowledge of the distribution of peak-to-total flux ratios,  $S_{\text{peak}}/S_{\text{total}}$ , as a function of source flux density. The form of this function is obviously dependent on the size of the beam but, in principle, can be derived from the distribution of source angular sizes. The shape of this distribution is controversial. Windhorst, Mathis & Neuschaefer (1990) claim that the integral distribution of angular source sizes (i.e., the fraction of sources larger than a given size  $\psi$ ) has the form

$$h(\psi) = 2^{-(\psi/\psi_{\text{med}})^{0.62}}, \quad (2)$$

where the median source size is given by

$$\psi_{\text{med}} = 2.0'' (S_{1.4}/1 \text{ mJy})^{0.3}, \quad (3)$$

while Bondi et al. (2003) claim that this overpredicts the number of large ( $\psi > 4''$ ) sources by a factor of  $\sim 2$ . While the Windhorst et al. parametrization is based on a small number of sources, we suspect that the difference is due, at least in part, to different beam sizes used by the authors. At sub-mJy flux densities, many radio sources comprise both a relatively compact component and more extended, diffuse emission and at high angular resolution, these components will be separated and the “angular size” determined from a fit to the compact component. At lower resolution, the entire source is likely to be well-fit by a single component and so the measured angular size will be larger. By convolving the distribution of source sizes with our beam, we can predict the distribution of peak-to-total flux ratios for sources with a given flux density, and we find that the Bondi et al. form for  $h(\psi)$  provides better agreement with our observations (Fig. 5).

Modifying Equation 1 to include only sources where the measured peak flux density exceeds our  $100\text{-}\mu\text{Jy}$  limit, based on the distribution of  $S_{\text{peak}}/S_{\text{total}}$ , allows us to properly determine the

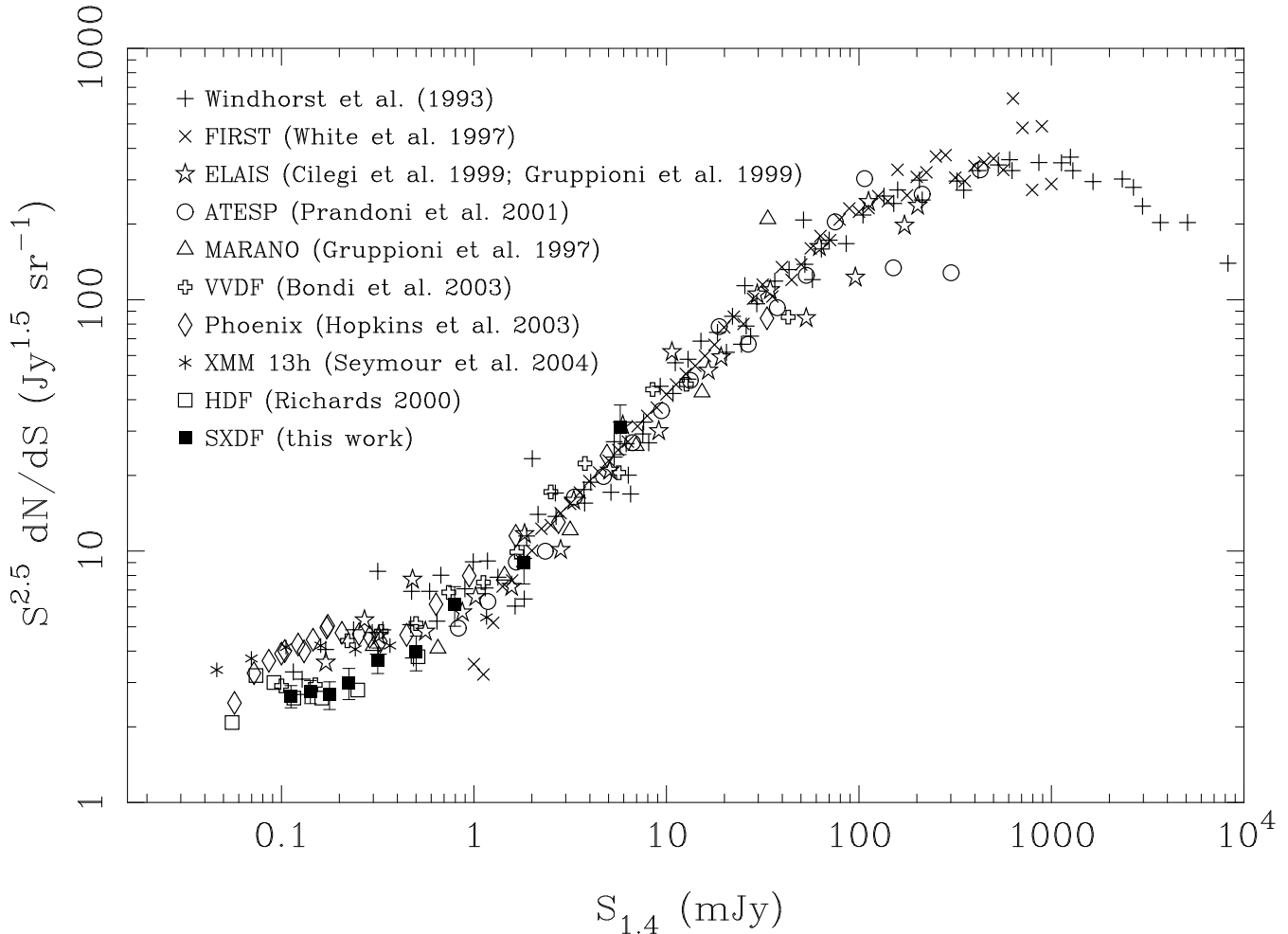


**Figure 6.** Differential source counts at 1.4 GHz from this work (solid symbols) and surveys in the literature: the compilation by Windhorst et al. (1993); FIRST survey (White et al. 1997); ELAIS (Cilegi et al. 1999; Gruppioni et al. 1999); ATESP (Prandoni et al. 2001); MARANO (Gruppioni et al. 1997); VLA-VIRMOS deep field (Bondi et al. 2003); Phoenix Deep Field (Hopkins et al. 2003); *XMM/ROSAT* 13-hour field (Seymour, McHardy & Gunn 2004); Hubble Deep Field North (Richards 2000).

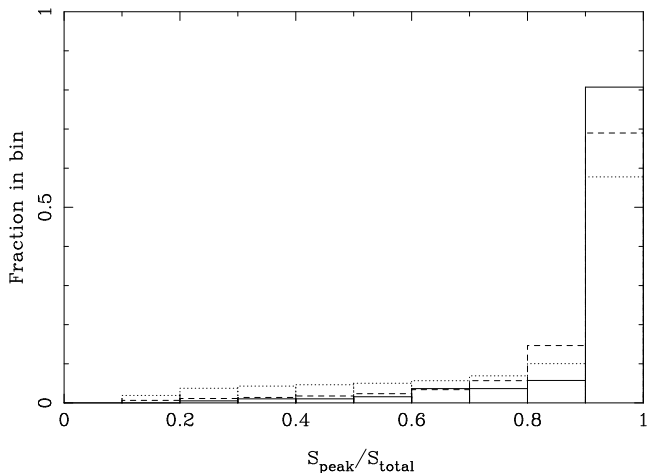


**Figure 5.** Histogram of peak-to-total flux ratio for the 192 sources with  $0.2 \leq S_t < 1.0$  mJy (solid line), compared with the predicted distribution assuming the angular size distributions of Bondi et al. (2003; dashed line) and Windhorst et al. (1990; dotted line). The predictions have been normalized to account for the incompleteness to very extended sources in our data.

**Table 2.** Source counts in the 100- $\mu$ Jy catalogue.

$S$ (mJy)	$\bar{S}$ (mJy)	$N$	Completeness	$S^{2.5}dN/dS$ ( $\text{Jy}^{1.5}\text{sr}^{-1}$ )
0.100–0.126	0.112	98	0.775	$2.67 \pm 0.27$
0.126–0.158	0.141	90	0.963	$2.77 \pm 0.29$
0.158–0.200	0.178	63	0.982	$2.68 \pm 0.34$
0.200–0.251	0.224	50	0.989	$2.99 \pm 0.42$
0.251–0.398	0.316	74	0.994	$3.69 \pm 0.43$
0.398–0.631	0.502	40	0.999	$3.97 \pm 0.63$
0.631–1.000	0.795	31	1.002	$6.12 \pm 1.10$
1.000–3.162	1.809	33	1.000	$8.96 \pm 1.56$
3.162–10.00	5.801	20	1.000	$31.18 \pm 6.97$

incompleteness corrections which need to be applied to our source counts. We adopt different forms for the true source counts to determine how sensitive the correction factors are to our assumed form for  $N(S)$ . We consider the sixth order polynomial of Hopkins et al. (2003), the third order polynomial of Katgert, Oort & Windhorst (1998), and a form where the source counts are flat in a Euclidian plot. The differences between these cases is negligible (less than one per cent), and we use the corrections derived from the Hop-

kins et al. parametrization. We also find that the correction factors are insensitive to the choice of angular size distribution and, while the use of the Windhorst et al. form does lead to an overestimation of the correction factors, this is only true when the factors are relatively small (at flux densities  $\sim 1.5$  times the detection threshold) and is not significant for a catalogue of our size. In the bin  $126 \leq S < 158 \mu\text{Jy}$ , for example, the completeness is calculated to be 91 per cent or 96 per cent for the Windhorst and Bondi models, respectively, and this difference only exceeds the Poisson uncertainty for a large catalogue with more than 400 sources in this range (our catalogue has only 90). At higher flux densities, the catalogue is essentially complete, while closer to the threshold, the correction factor is determined by the fraction of resolved sources which, for our beam size, is close to the median source size (which is the same for both angular size distributions). The completeness is higher if the functional form of Bondi et al. scales with the median angular size, but even then the difference is less than 10 per cent and still comparable with the Poissonian uncertainty. Deep A-array data (Ivison et al. 2006) have been taken in the central region of the SXDF to identify submillimetre sources detected in the SCUBA Half-Degree Extragalactic Survey (SHADES; Mortier et al. 2005), and this will allow us to determine more accurately the angular size distribution of sources at  $\sim 100 \mu\text{Jy}$  levels, which we will do in a later paper. At the present time, we determine correction factors to the observed source counts from the Bondi et al. form for the angular size distribution, assuming this does not change with flux density. The sources are grouped in bins of flux density of width  $\Delta \log S = 0.1$  at the lowest flux densities, with an increasing bin size as the numbers decrease towards higher fluxes. The centre of each bin was calculated from equation 19 of Windhorst et al. (1984) where the slope of the source counts was iteratively determined by interpolating between the adjacent bins. The raw source counts and correction factors are given in Table 2, while the differential counts are presented in Fig. 6.

We note that there is almost a factor of two peak-to-peak variation in the observed number counts at a flux density of  $\sim 200 \mu\text{Jy}$  between the different surveys plotted in Fig. 6. The SXDF points lie at the low extreme, but are consistent with those measured from the HDF, VVDF, and Windhorst et al. (1990, 1993) surveys. The Phoenix Deep Survey (Hopkins et al. 2003) has higher number counts, despite covering approximately one square degree (the *XMM-Newton* 13-hour survey and ELAIS surveys also produce much higher number counts, but cover significantly smaller areas). Although the restoring beam used by Hopkins et al. is nearly four times larger in area than ours (whereas the SXDF and VVDF use restoring beams of similar size), the source density at these flux limits is still too low for source confusion to be an important effect. We can also rule out the possibility that we are missing diffuse sources which are seen with a larger beam, since (i) the Windhorst et al. surveys use an even larger beam, and (ii) we have corrected for sources with peak flux densities below our limit, and so have a good measurement of the total number of sources with  $S > 100 \mu\text{Jy}$ . With  $\sim 100$  sources per flux density bin, the statistical uncertainty is  $\sim 10\%$ , while we can estimate the effects of cosmic variance using the method of Somerville et al. (2004). Assuming that faint radio sources have the same correlation length as mJy sources from the FIRST and NVSS surveys ( $r_0 \approx 5 \text{ Mpc}$ ; Overzier et al. 2003) and sample the redshift interval  $z = 1 \pm 0.5$ , the r.m.s. uncertainty from cosmic variance is estimated to be  $\sim 9\%$  (equation 3 of Somerville et al.). A similar value is obtained if a bias of  $b \approx 2$  (e.g., Peacock & Dodds 1994) is assumed for the radio sources.

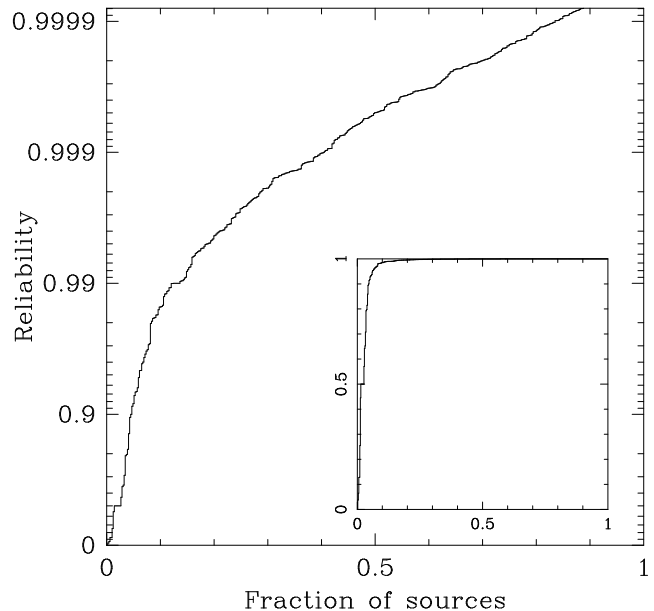


**Figure 7.** Histogram showing the fraction of sources with reliability measurements (Sutherland & Saunders 1992) above a given value. The inset shows the same plot with a linear  $y$ -axis. Not included in this figure are 7 sources where the optical identification is obscured by a bright foreground object. The 15 sources whose radio morphologies made the reliability measurement an inappropriate statistic have been assigned values of 0.99, 0.9, and 0.5 if their identifications are considered *reliable*, *probable*, and *plausible*, respectively.

The extrema of the source counts plotted in Fig. 6 may therefore represent  $\pm 2\sigma$  deviations from the mean number density.

## 4 OPTICAL IDENTIFICATIONS

### 4.1 Assignment of optical counterparts

We have attempted optical identifications of the radio sources from the ultra-deep  $BRi'z'$  Suprime-Cam images of the SXDF. These are described in detail by Furusawa et al. (2006). Seven sources lie outside the region covered by these data, and for these sources we have used shallower unpublished  $R$  and  $i'$  images from Suprime-Cam.

We first confirm the astrometry by comparing the radio and optical ( $R$ -band) positions of those sources with unresolved (or barely-resolved) morphologies in both bands. We select the 20 brightest such radio sources (all with peak signal-to-noise ratios greater than 15) and find that the mean offsets in right ascension and declination between the centroids in the two images are 0.03 and 0.24 arcsec, respectively (with the optical IDs lying to the southwest of the radio sources). Since these are both much smaller than the size of the radio beam, we do not make any corrections to the astrometry of either the optical or the radio images.

Likely identifications were then made for all sources by overlaying the radio contours onto a true-colour  $BRz'$  image of the field around each radio source. A 2-arcminute field was used to ensure that all possible double radio sources were identified. The relatively high resolution of the radio imaging made most identifications unambiguous, since there was typically only one source within an arcsecond of the peak of the radio emission, even at extremely faint optical magnitudes. In instances where more than one optical coun-

terpart was visible, blue unresolved sources (often identified with X-ray sources from the catalogue of Ueda et al. 2006) or faint red resolved objects were favoured. For cases where a source was composed of multiple radio components but no core was visible, an identification was sought in the centre of the source.

Once an optical counterpart had been identified, it was matched to an object in the Version 1 catalogue from the optical imaging. Usually, a counterpart was found in the  $R$ -band catalogue, but occasionally the object was blended and a different band had to be used. In some cases, the proposed ID was blended in all the catalogues, in which case SExtractor was re-run over the Suprime-Cam image with a more severe deblending threshold.

We investigate the reliability of our optical identifications using the criterion of the likelihood ratio as defined by Wolstencraft et al. (1986), after de Ruiter, Arp & Willis (1977), and developed by Sutherland & Saunders (1992) for cases where there may be more than one possible identification for a given source. For each radio source  $r$ , likelihood ratios  $L_{or}$  are calculated for all optical sources  $o$  within 5 arcsec of the radio position, using the formula

$$L_{or} = \frac{Q(< m_o) \exp(-r_{or}^2/2)}{2\pi\sigma_x\sigma_y N(< m_o)}. \quad (4)$$

Here,  $Q(< m_o)$  is the fraction of radio sources whose optical counterparts are brighter than that of the proposed optical ID (we estimate this in an iterative fashion from our own catalogue);  $\sigma_x$  and  $\sigma_y$  are the combined (radio plus optical) 1-sigma uncertainties in the positions along the major and minor axes of the restored beam, respectively, calculated as  $\sigma_x = \sqrt{(0.45\theta_x/\text{SNR})^2 + 0.29^2}$  (and similarly for  $\sigma_y$ ) using the formula of Reid et al. (1988) and adding in quadrature the standard deviation measured from the radio-optical offsets.  $r_{or} = \sqrt{(\Delta x/\sigma_x)^2 + (\Delta y/\sigma_y)^2}$  is the normalized separation between the radio and optical positions, and  $N(< m_o)$  is the surface density of objects brighter than the proposed optical ID (determined from the Suprime-Cam catalogues). We apply the offset measured between the radio and optical astrometric frames before calculating the separation between the radio and optical positions. The analysis is performed in the filter in which the initial identification was made (i.e., usually the  $R$ -band).

The probability that a particular optical object  $i$  is the correct identification for a radio source (the reliability) is then given by

$$\mathcal{R}_i = \frac{L_{ir}}{\sum_o L_{or} + (1 - Q)} \quad (5)$$

(Sutherland & Saunders 1992), where  $Q$  is the fraction of radio sources with optical counterparts, which we estimate to be 95 per cent from our data (i.e., the fraction of sources with  $\mathcal{R} \leq 0.5$ , although the vast majority of the identifications are insensitive to this value). Of our 505 sources, 7 cannot be identified due to the presence of a bright foreground star or galaxy, while a further 15 have extended radio morphologies for which the radio position may not be indicative of the location of the optical counterpart. In 13 of these cases, we assign optical identifications based on our experience studying extragalactic radio sources and label these identifications as *reliable* (5), *probable* (1), or *plausible* (6). One more (VLA 0016) has two possible IDs, while two (VLA 0017 and VLA 0049) have *certain* optical counterparts. All these sources are presented in the Appendix. Formal probabilities can be assigned to the proposed optical counterparts of the remaining 483 radio sources by the above method. We assign as the *primary* optical counterpart the source with the largest reliability, but in the cat-

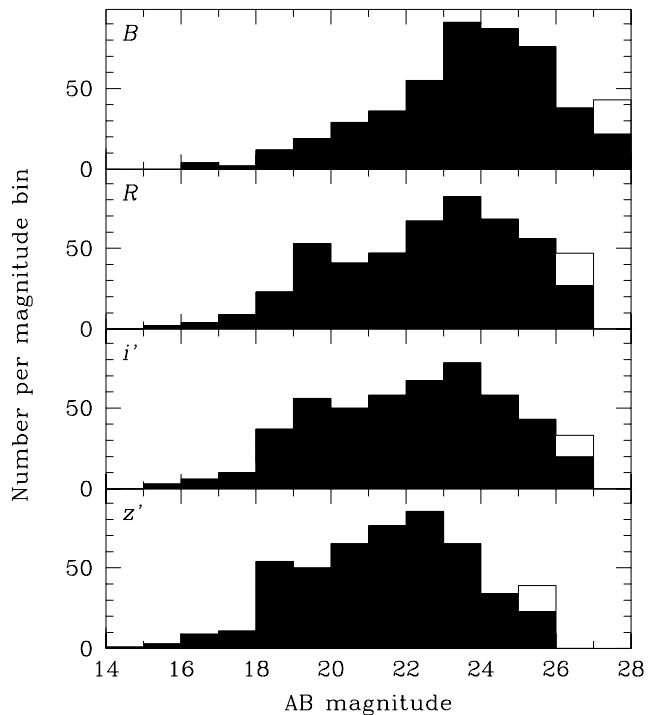


**Figure 8.** Magnitude distributions for the identifiable radio sources. The open region in the faintest magnitude bin (the last bin where the completeness of the optical catalogue is still high) indicates objects with magnitudes fainter than this bin. In addition to the 7 sources whose identification is hampered by the presence of bright foreground objects, a further seven sources lie outside the multicolour SXDF imaging and only appear in the  $R$  and  $i'$  histograms.

alogue we list all counterparts with  $\mathcal{R} > 0.05$ . The catalogue is available on the world wide web and a portion is shown in Table 3.

Fig. 7 shows the cumulative distribution of reliability measurements for all 498 sources not affected by foreground objects. A total of 459 sources have probabilities of  $>90$  per cent of having been correctly identified (plus a further 6 are *reliably* classified by eye, while 2 more have *certain* identifications) and, after the sorting the objects with numerically-assigned reliabilities in order of decreasing probability, there is a less than 50 per cent chance of *any* of the first 436 sources being incorrectly identified. In the Appendix, we present radio-optical overlays of the extended radio sources and those where we have made an identification which has a low formal probability.

Our optical identification fraction of  $\sim 90\%$  (for sources with  $\mathcal{R} \geq 0.9$  reduces by a factor of more than 2 the percentage of ‘blank field’ sources, compared to other surveys with shallower optical limits (e.g., Sullivan et al. 2004; Ciliegi et al. 2005). This can be naturally explained as being due to the greater depth of our optical imaging. On the other hand, we also have a higher identification fraction than Afonso et al. (2006) determined for faint radio sources in the GOODS-S field using *Hubble Space Telescope* Advanced Camera for Surveys (ACS) imaging. Of the 37 radio sources with  $S_{1.4} \geq 100 \mu\text{Jy}$ , they fail to find optical identifications for 6 (16%), down to very deep limits  $z' \approx 28$ , while a further two lie in the optical magnitude range  $25.5 < z' < 28$  (i.e., between the limiting magnitudes of our data and the ACS data). The relatively low identification fraction of Afonso et al. is not readily explicable considering that it is no higher than for optical surveys which are 3-4 magnitudes shallower. The distributions of optical magnitudes



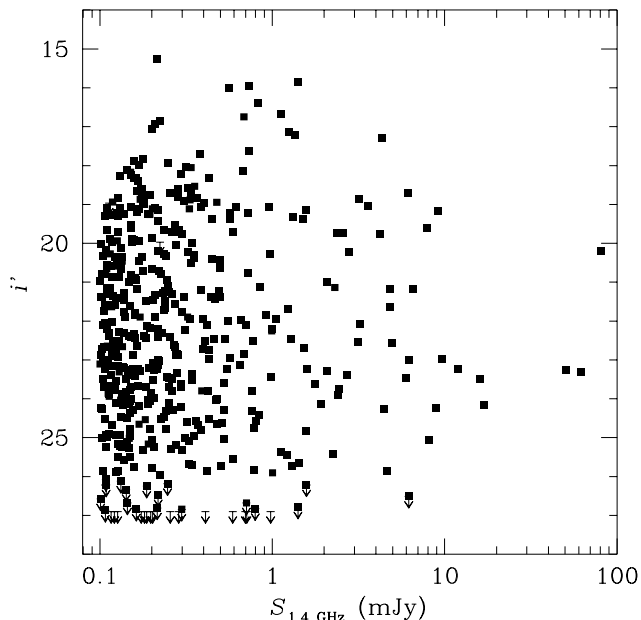


**Figure 9.** Optical ( $i'$ ) magnitude vs radio flux density for all sources not contaminated by bright foreground objects. Upper limits indicate sources with no counterpart or whose identifications have  $\mathcal{R} < 0.01$ .

of our identifications are shown in Fig. 8. Fig. 9 plots the  $i'$  magnitude against radio flux density, and it can be seen that there is no strong correlation between these two variables.

Colour-colour plots for our sources were constructed, in three different bins of radio flux density. These are shown in Fig. 10, and compared to evolutionary tracks for elliptical and spiral galaxies and a (non-evolving) QSO spectrum. Although it is clear from these figures that photometric redshifts can be determined for many of the radio sources from their optical colours alone, we defer discussion of this to a later paper, for three reasons. First, a photometric redshift code is being developed (Furusawa et al., in preparation) which will use already-obtained spectroscopy of galaxies in the SXDF as a training set to improve its accuracy. Second, deep near-infrared imaging data will be obtained in the very near future as part of the UKIDSS UDS (Lawrence et al. 2006), and it has been demonstrated that photometric redshifts are consistently more reliable with the inclusion of such data (e.g., Connolly et al. 1997). Finally, extensive spectroscopy has been obtained using VLT/VIMOS and we expect this to yield spectroscopic redshifts for a large fraction of the sources; we therefore believe it is of little benefit to derive photo- $z$ 's for our sources at this juncture.

## 4.2 Nature of the faint radio source population

As Fig. 6 clearly shows, there is a dramatic change in the slope of the source counts at flux densities below about 1 mJy, suggesting the emergence of a new population of radio sources. Historically, it has been assumed that this new population is low-to-moderate redshift star forming galaxies, and the overall distribution has been successfully modelled with a suitable parametrization of the evolution of these objects (e.g., Seymour et al. 2004). However, there is no strong observational evidence to support this as there has been limited optical identification of these sources. Jarvis & Rawlings (2004) have made the alternative suggestion that the new population comprises radio-quiet AGNs. Although we have spectroscopic

**Table 4.** Comparison of the colour-colour plots shown in Fig. 10. Column and rows indicate the radio flux density ranges of the two samples being compared. The numbers are the probabilities that the null hypothesis (that the two samples have the same distribution) is correct, using the two-dimensional Kolmogorov–Smirnov test of Peacock (1983), with the upper-right being for  $BRz'$  colours and the lower-left for  $Bi'z'$ . The parenthesized values indicate where the probability estimation is unreliable.

	100–150	150–300	>300
100–150	...	0.144	(0.791)
150–300	0.113	...	0.197
>300	(0.621)	0.102	...

redshifts for only a few radio sources in the SXDF, the extremely high identification fraction allows us to compare the photometric properties of the radio source IDs at different radio flux densities.

We use the two-dimensional Kolmogorov–Smirnov test (Peacock 1983) to investigate differences between pairs of colour-colour distributions shown in Fig. 10, and summarize our results in Table 4. It is clear that there is no significant change in the properties of the optical IDs with radio flux density. We stress that this result is robust and not dependent on the choice of bins; for example, there is no statistically significant difference (even at 80 per cent confidence) between the properties of radio sources with  $100 \mu\text{Jy} \leq S_{1.4} < 120 \mu\text{Jy}$  and  $S_{1.4} > 1 \text{ mJy}$ . All three bins show a significant number of both blue and red objects, although the central flux density bin has a larger fraction of blue objects and is more dissimilar from the other two bins than they are from each other. This argues against there being a gradual change in the composition of the radio source population as one moves to fainter flux densities, as would be expected if starburst galaxies became increasingly dominant. Since we know that the bright radio sources are predominantly passively-evolving massive elliptical galaxies (e.g., Willott et al. 2003), many of the faint radio sources must also be ellipticals.

We investigate further by comparing the radio and X-ray properties of our radio sources. We use the X-ray catalogue of Ueda et al. (2006) and apply the same detection thresholds as Akiyama et al. (2006), namely that a source must have a likelihood  $\mathcal{L} \geq 9$  in one of the 0.3–10 keV (total), 0.5–2 keV (soft), or 2–10 keV (hard) bands. These are fairly conservative criteria in the sense that only 3 spurious sources are expected in the total band sample per *XMM-Newton* pointing. We search for the X-ray source nearest to the position of each optical counterpart (or the radio position if there is no optical counterpart), and find the distribution of optical–X-ray separations shown in Fig. 11. From this Figure, we decide to consider radio and X-ray sources to be counterparts if the separation is less than 5 arcseconds, which results in 60 radio–X-ray matches (i.e.,  $11.9 \pm 1.4\%$  of the radio source population), of which 6 are expected to be chance associations. None of our X-ray matches has a significant spatial extent.

Relationships have been determined between the star formation rate (of stars with  $M > 5M_{\odot}$ ) and the radio and X-ray luminosities of star-forming galaxies: (Condon 1992; Ranalli, Comastri & Setti 2003), which can be combined to determine the relationships between radio and X-ray luminosities for star-forming galaxies. Since the spectral shapes in the radio and X-ray regimes are very similar ( $S_{\nu} \propto \nu^{-0.8}$ ), these can be used to derive a correlation between fluxes which can be applied to our data where redshifts (and hence luminosities) are unknown. The relationships are:

$$S_{0.5-2\text{keV}} (\text{W m}^{-2}) = 10^{-18.0} S_{1.4\text{GHz}} (\text{mJy}) \quad (6)$$

**Table 3.** The 100  $\mu\text{Jy}$  catalogue (only the first 20 sources are shown). The full catalogue, containing brief notes for many sources plus additional information, is available via the world wide web at <http://www.astro.ljlm.ac.uk/~cjs/SXSDS/radio/>, or from the authors on request. Where a number is not listed in the Reliability column, A, B, and C represent *reliable*, *probable*, and *plausible*, respectively, while a dash indicates a *certain* identification. The list is sorted in order of decreasing flux density, and the quoted uncertainties are those arising from the limited signal-to-noise ratio of the map, ignoring calibration errors (we note from Fig. 3 that our flux density scale agrees well with that of the NVSS for the brightest sources, where such calibration errors will be most important).

No.	Name	Radio position (J2000.0)		$S_{1.4\text{ GHz}}$ ( $\mu\text{Jy}$ )	Reliability	Catalogue ID	Optical position (J2000.0)		$z_{\text{spec}}$	$B$	$V$	$R$	$i'$	$z'$
0001	VLA J021827–04546	2:18:27.32	–4:54:37.29	80250.0 $\pm$ 72.8	A	RC–124990	02:18:27.161	–04:54:41.60		23.1069	21.9154	20.9715	20.2001	19.7440
0002	VLA J021817–04461	2:18:18.16	–4:46:07.23	62110.0 $\pm$ 63.9	0.9998	zN–018551	02:18:18.139	–04:46:07.55		26.0638	25.2152	24.3091	23.3194	22.4120
0003	VLA J021839–04418	2:18:39.53	–4:41:50.10	50820.0 $\pm$ 70.9	A	RN–045293	02:18:39.559	–04:41:49.57		23.2065	23.2808	23.4545	23.2485	22.9986
0004	VLA J021853–04475	2:18:53.64	–4:47:35.09	16950.0 $\pm$ 67.6	0.2545	RC–181189	02:18:53.587	–04:47:36.29		24.9128	24.0525	24.4167	24.1701	23.5582
0005	VLA J021851–05090	2:18:51.34	–5:09:00.60	16010.0 $\pm$ 65.9	0.9816	RC–034792	02:18:51.326	–05:09:01.53		24.5141	23.9246	23.9683	23.4888	22.9546
0006	VLA J021637–05154	2:16:37.86	–5:15:28.15	12020.0 $\pm$ 77.1	0.9993	zW–000000	02:16:37.825	–05:15:28.28		24.2747	23.8249	23.4450	23.2288	22.7383
0007	VLA J021659–04493	2:16:59.02	–4:49:20.53	9600.0 $\pm$ 135.0	A	RC–160974	02:16:59.064	–04:49:20.85	1.324	25.0818	24.6208	23.9604	22.9805	22.0174
0008	VLA J021823–04530	2:18:23.99	–4:53:04.10	9150.0 $\pm$ 57.3	0.9958	RC–132441	02:18:24.005	–04:53:05.23	0.341?	20.5376	19.8146	19.3770	19.1677	18.9268
0009	VLA J021803–05384	2:18:03.37	–5:38:25.00	8910.0 $\pm$ 91.5	0.9938	RS–004164	02:18:03.420	–05:38:25.43		26.1566	24.5809	24.5523	24.2270	24.6911
0010	VLA J021850–04585	2:18:50.55	–4:58:32.00	8120.0 $\pm$ 61.3	0.9322	RC–103643	02:18:50.491	–04:58:32.31		26.4387	24.5014	25.8306	25.0711	24.1989
0011	VLA J021823–05250	2:18:23.52	–5:25:00.44	7950.0 $\pm$ 97.2	1.0000	RS–087802	02:18:23.532	–05:25:00.69	0.644	22.5712	21.3233	20.4645	19.5930	19.1252
0012	VLA J021634–04550	2:16:34.99	–4:55:05.61	6590.0 $\pm$ 156.0	0.9986	RW–058187	02:16:34.968	–04:55:06.47		24.8528	23.4401	22.2077	21.1867	20.4675
0013	VLA J021616–05128	2:16:16.82	–5:12:53.47	6250.0 $\pm$ 89.6	0.9999	RW–086319	02:16:16.822	–05:12:53.71	2.710	23.6996	23.0319	23.1279	23.0045	22.6839
0014	VLA J021752–05053	2:17:52.135	–5:05:21.25	6190.0 $\pm$ 45.6	0.9653	RC–059317	02:17:52.118	–05:05:22.23		30.1862	27.2512	26.8674	26.5090	25.8446
0015	VLA J021932–05075	2:19:32.20	–5:07:32.66	6100.0 $\pm$ 117.5	A	RE–068363	02:19:32.201	–05:07:32.67	0.344	20.5793	19.4431	18.9311	18.7136	18.4210
0016	VLA J021826–04597	2:18:26.15	–4:59:46.25	5950.0 $\pm$ 83.8	B	RC–095238	02:18:25.958	–04:59:45.58	1.132	24.2799	23.8575	23.8548	23.4662	22.9034
					C	RC–095351	02:18:26.088	–04:59:46.76		25.3795	24.6803	24.3634	23.8498	23.4315
0017	VLA J021827–05348	2:18:27.57	–5:34:53.77	4970.0 $\pm$ 81.3	–	RS–026242	02:18:27.312	–05:34:57.40	2.579	22.7569	22.4935	22.4985	22.5523	22.0505
0018	VLA J021724–05128	2:17:24.38	–5:12:51.68	4840.0 $\pm$ 146.3	0.9946	RS–174900	02:17:24.415	–05:12:52.63	0.918	23.9318	22.8145	22.1173	21.1717	20.2797
0019	VLA J021757–05279	2:17:57.26	–5:27:55.82	4830.0 $\pm$ 115.5	B	RS–070109	02:17:57.288	–05:27:55.88	0.694	21.9134	21.7338	22.4154	21.6429	21.0130
0020	VLA J021800–04499	2:18:00.68	–4:49:54.78	4600.0 $\pm$ 83.0	C	zC–000000	02:18:00.716	–04:49:56.41		27.4331	26.6552	26.6517	25.8663	25.0541

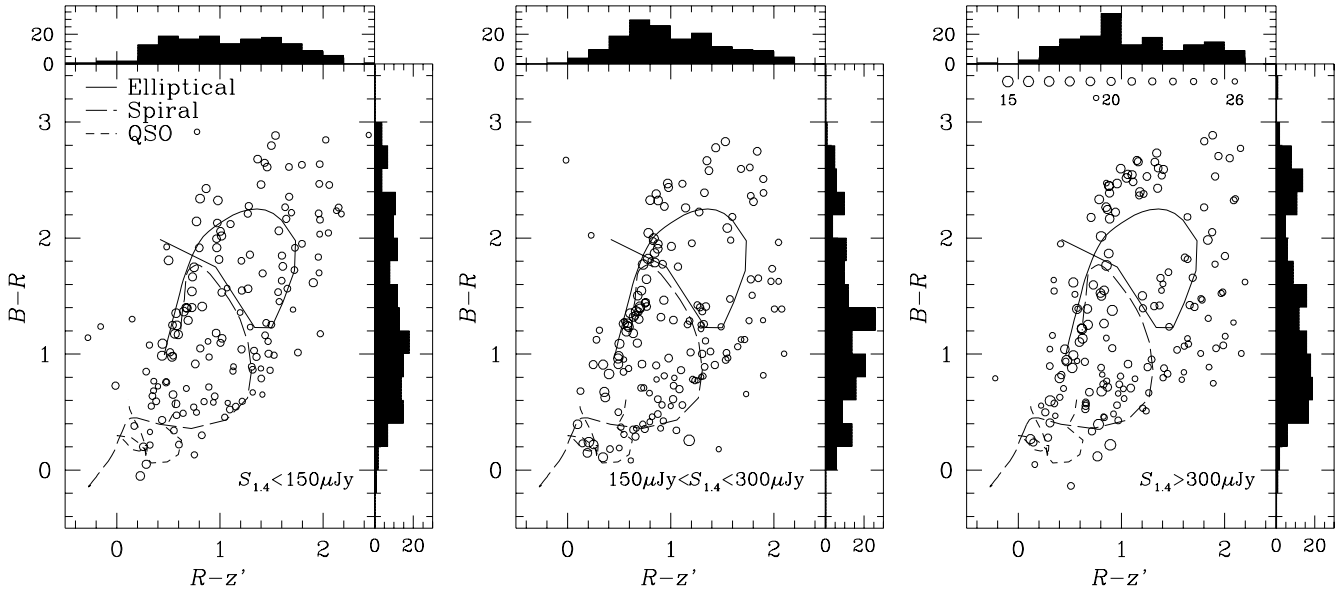


**Figure 10.** Colour–colour plots for the radio source IDs, in different radio flux density ranges. The sizes of the symbols represent the optical ( $R$ -band) magnitudes of the sources (larger symbols represent brighter sources as shown in the right-hand panel), and the three curves show the tracks for elliptical and spiral galaxies, and a (non-evolving) QSO in the range  $0 < z < 3$ . The galaxy tracks were computed using Version 2.0 of the PEGASE code (Fioc & Rocca-Volmerange 1997). The elliptical galaxy was modelled as an instantaneous burst at  $z = 5$ , while the spiral galaxy formed at  $z = 3$  and had an exponentially-decaying star formation rate. In both cases, a Kroupa (2001) initial mass function was adopted and extinction was added assuming a spheroidal geometry. The QSO track was derived from the Sloan Digital Sky Survey composite spectrum (Vanden Berk et al. 2001). The histograms show the distribution of colour along each axis.

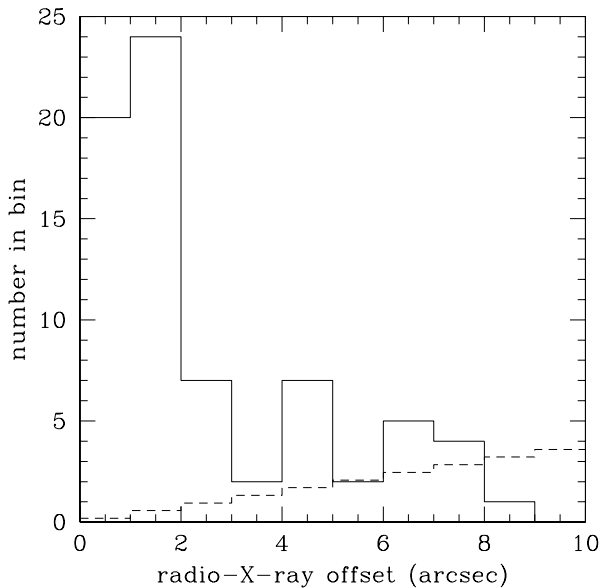


**Figure 11.** Histogram of the separations between the locations of the optical counterparts of radio sources and the X-ray sources to which they have been matched. The dashed line shows the expectation of chance associations assuming the X-ray sources are distributed uniformly on the sky. We consider sources to be associated if the separation is  $< 5''$ .

$$S_{2-10\text{keV}} (\text{W m}^{-2}) = 10^{-18.0} S_{1.4\text{GHz}} (\text{mJy}) \quad (7)$$

Correlations between X-ray and radio luminosities for radio-quiet AGNs have been determined by Brinkmann et al. (2000). These are very close to being proportionalities, and so we can con-

vert them to relationships between fluxes:

$$S_{0.5-2\text{keV}} (\text{W m}^{-2}) = 10^{-15.5} S_{1.4\text{GHz}} (\text{mJy}) \quad (8)$$

$$S_{2-10\text{keV}} (\text{W m}^{-2}) = 10^{-15.3} S_{1.4\text{GHz}} (\text{mJy}) \quad (9)$$

We also consider the correlation which is present between the radio core and X-ray luminosities for low-power (FR I) radio galaxies (Canosa et al. 1999; FR II radio sources would need to lie at  $z > 4$  to be this faint). Hardcastle & Worrall (2000) have attributed this to an inverse Compton origin for the X-ray emission. If we assume that our measured radio flux densities are dominated by the flat spectrum core components of FRI radio galaxies, we expect them to obey the following correlations:

$$S_{0.5-2\text{keV}} (\text{W m}^{-2}) = 10^{-19.3} (1+z)^{-0.8} S_{1.4\text{GHz}} (\text{mJy}) (10)$$

$$S_{2-10\text{keV}} (\text{W m}^{-2}) = 10^{-19.1} (1+z)^{-0.8} S_{1.4\text{GHz}} (\text{mJy}) (11)$$

Only the brightest, most nearby sources would be detected in the SXDF X-ray images, which have a flux limit of  $\sim 10^{-18} \text{ W m}^{-2}$ , and we do not consider this mechanism further.

We plot the soft and hard X-ray fluxes (computed assuming an X-ray photon index  $\Gamma = 1.8$ ) of the 60 X-ray-detected radio sources versus radio flux density in Fig. 12. It is immediately clear from these plots that a population of X-ray bright radio sources appears at radio fluxes  $S_{1.4} \lesssim 300 \mu\text{Jy}$ , i.e., where the new population of radio sources starts to dominate. The ratios of X-ray flux to radio flux density of these sources indicate that they are radio-quiet AGNs.

The optical morphologies of these objects provide further clues as to their nature. We use the SExtractor CLASS\_STAR field (Bertin & Arnouts 1996) to determine whether the objects are point-like or resolved in the  $i'$ -band, using a value of 0.8 as the borderline. Fig. 12(a) shows that most objects which are bright in the soft X-ray band are point-like, and so are almost certainly radio-

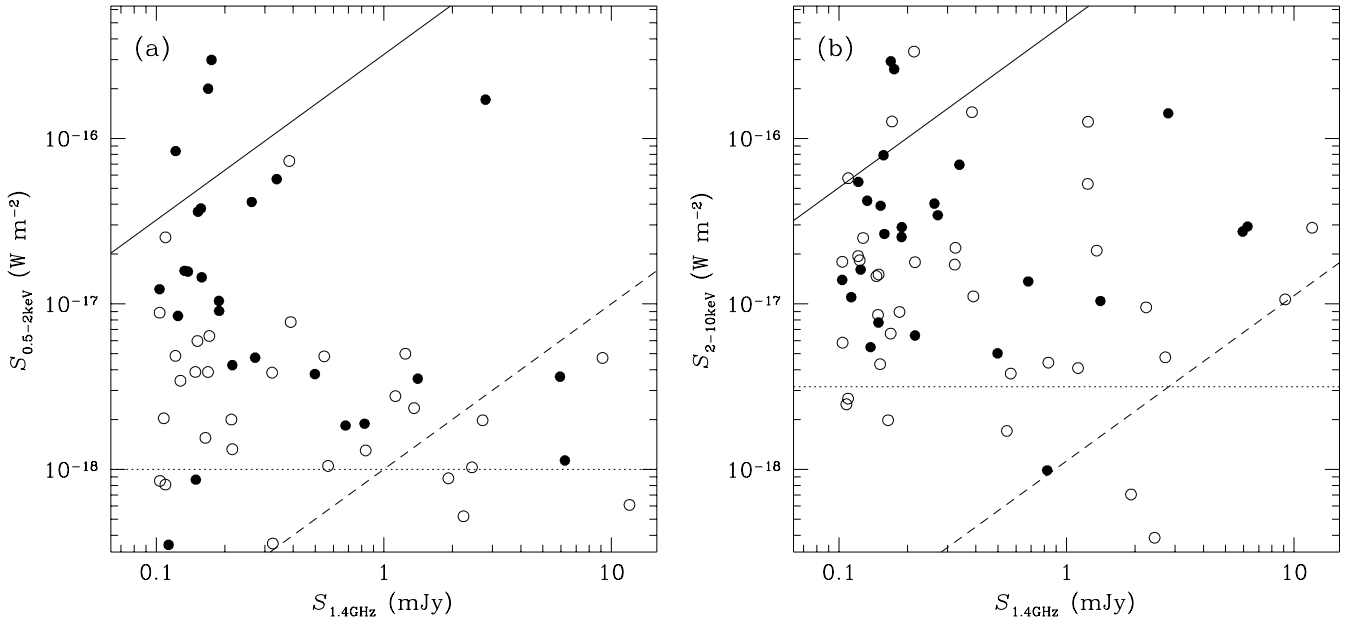


**Figure 12.** Plots of (a) soft and (b) hard X-ray flux vs radio flux density for the radio sources with X-ray detections. Filled symbols represent optical point sources and open symbols optically extended objects. In each plot, the dashed line indicates the relationship for starburst galaxies (Eqns 6–7) while the solid line shows the correlation for radio-quiet AGNs (Eqns 8–9). Most (88 per cent) of the radio sources are not detected in X-rays; we show the approximate limits of the X-ray data (Akiyama et al. 2006) by the dotted lines in each figure.

quiet QSOs which suffer little obscuration at either optical or X-ray wavelengths. In Fig. 12(b), however, many of the hard-X-ray-bright objects are resolved optically and are therefore likely to be ‘Type 2’ objects, where the nucleus suffers significant obscuration.

If we assume that objects in Fig. 12(b) are radio-quiet AGNs or starbursts according to which of the two correlations they are closer to, we can determine that at least 10 per cent of radio sources with  $S_{1.4} < 300 \mu\text{Jy}$  are radio-quiet AGNs. This fraction is the same in the bins of radio flux density 100–150  $\mu\text{Jy}$  and 150–300  $\mu\text{Jy}$ , and is a lower limit since there are two effects which can cause objects to migrate towards the bottom-right of this plot: relativistic effects can boost the radio flux of a source whose jets are oriented close to the line of sight, and photoelectric absorption can significantly reduce the observed X-ray flux. With regard to the first point, Falcke, Sherwood & Patnaik (1996) suggest that  $\sim 10$  per cent of radio-quiet QSOs may have their core radio fluxes (and hence their overall radio fluxes) enhanced by Doppler boosting. Regarding the second point, the 2–10 keV count rate from an AGN at  $z = 0.7$  is reduced by an order of magnitude for an absorbing column  $N_{\text{H}} = 1.5 \times 10^{24} \text{ cm}^{-2}$ , and the fraction of such Compton-thick AGNs has been estimated to be 20–30 per cent of the total, both from observations of local Seyfert galaxies (Risaliti, Maiolino & Salvati 1999), and from fits to the Cosmic X-ray Background (Ueda et al. 2003). Furthermore, the correlations between radio and X-ray luminosity used above were derived from cross-correlation of a deep radio catalogue and a shallower X-ray catalogue, and will therefore be biased towards unusually X-ray-luminous sources. The true correlations for radio-quiet AGNs could be significantly lower in Fig. 12 and the fraction of sources which lie close to it may have been underestimated as a result. Indeed, this seems very likely since the solid lines in Fig. 12 clearly exceed the median X-ray fluxes of the QSOs. Our ongoing follow-up of both radio- and X-ray-selected samples in the SXDF will enable an investigation of the correlations between X-ray and radio luminosi-

ties without such biases. We tentatively suggest that 20 per cent or more of the radio sources with  $100 \mu\text{Jy} \leq S_{1.4} < 300 \mu\text{Jy}$  are radio-quiet AGNs. Models for the evolution of the radio luminosity function indicate that, despite their faintness, approximately half of the radio sources at these flux densities are radio-loud AGNs (e.g., Jarvis & Rawlings 2004; this conclusion rests on the assumption that there is not a strong cut off in the space density of low-power FR I radio sources at  $z \lesssim 1$ ), and therefore radio-quiet AGNs may provide a larger fraction of the flattening signal than starburst galaxies.

This has clear implications for studies of the Cosmic X-ray Background (CXB), as alluded to by Jarvis & Rawlings (2004). These authors considered the reverse calculation, using the hard X-ray luminosity function of Ueda et al. (2003) to predict the contribution from radio-quiet AGNs to the radio source counts at faint flux densities. From their fig. 3,  $\sim 10$ –15 per cent of radio sources with  $100 \mu\text{Jy} \leq S_{1.4} < 300 \mu\text{Jy}$  are radio-quiet AGNs, which is in agreement with our lower limit. However, if there is a population of Compton-thick AGNs, these will not be seen in the 2–10 keV source counts of Ueda et al., and hence Jarvis & Rawlings have also calculated a lower limit to the radio-quiet AGN fraction at faint radio flux densities. While such Compton-thick objects do not contribute much of the 2–10 keV background light, they will not be as strongly absorbed at the  $\sim 30$  keV peak of the CXB. Ueda et al.’s (2003) model of the CXB has a knee in the 30 keV source counts where most of the background is produced, and these objects have intrinsic 2–10 keV fluxes near the observed knee in the 2–10 keV counts at  $S_{2-10\text{keV}} \approx 2 \times 10^{-17} \text{ W m}^{-2}$ , or  $S_{1.4} \approx 40 \mu\text{Jy}$ . While the observed X-ray flux may be reduced by a large (possibly Compton-thick) absorption column, the radio flux will remain unaffected, and hence radio surveys to this depth can identify the objects which dominate at the 30 keV peak of the CXB, *even if they are Compton-thick and invisible to deep X-ray surveys*. While this radio-quiet AGN population will be contaminated by star-forming

galaxies, it can be expected that colour-selection criteria will allow discrimination between these two populations (e.g., by using the *Spitzer*/IRAC bands to detect the AGN-heated dust at  $T \sim 1000$  K which is not present in starburst galaxies), and hence separate the much brighter (at X-ray energies) AGNs from the starbursts. One can hence determine unambiguously whether a population of intrinsically luminous obscured high-redshift radio-quiet AGNs does exist, even if they are too faint for current X-ray telescopes. This is in marked contrast to the results from deep X-ray surveys, where the increased depth has resulted in the detection of low-redshift, apparently intrinsically faint, AGNs (e.g., fig. 5 of Barger et al. 2003), rather than the hoped-for higher redshift population. It is possible that some fraction of the faintest X-ray sources are Compton-thick objects where only scattered radiation is being seen at 2–10 keV, but there is no definitive way to test this except to measure the X-ray fluxes at higher energies. We will study the multiwavelength properties of the faint radio sources in a later paper.

## 5 SUMMARY

We have presented a radio map covering 1.3 square degrees in the region of the Subaru/*XMM-Newton* Deep Field, and described the production of a catalogue covering 0.81 square degrees containing all sources with a peak flux density greater than  $100 \mu\text{Jy beam}^{-1}$ . We have made reliable identifications for 90 per cent of the sources, which is a significantly higher fraction than other surveys covering a similar area. We have demonstrated that there is no significant difference between the optical colours of radio sources selected at different flux densities, and have combined this with X-ray data to show that an important fraction of the faint ( $100 \mu\text{Jy} \leq S_{1.4} < 300 \mu\text{Jy}$ ) radio source population must be radio-quiet AGNs, including Type 2 objects which contribute to the Cosmic X-ray Background.

## ACKNOWLEDGMENTS

This paper is partially based on data collected at Subaru Telescope, which is operated by the National Astronomical Observatory of Japan. The National Radio Astronomy Observatory is a facility of the National Science Foundation operated under cooperative agreement by Associated Universities, Inc. CS and SR thank the Particle Physics and Astronomy Research Council for funding in the form of an Advanced Fellowship and Senior Research Fellowship, respectively. The authors thank Nick Seymour for providing the data used to produce Fig. 6, and the referee, Jim Condon, for numerous helpful comments.

## REFERENCES

Afonso J., Mobasher M., Koekemoer A., Norris R. P., Cram L., 2006, *AJ*, 131, 1216  
 Akiyama M., Ueda Y., Sekiguchi K., Takata T., Yoshida M., Simpson C., Watson M., 2006, in preparation  
 Barger A. J., et al., 2003, *AJ*, 126, 632  
 Benn C. R., Rowan-Robinson M., McMahon R. G., Broadhurst T. J., Lawrence A., 1993, *MNRAS*, 263, 98  
 Bertin E., & Arnouts S., 1996, *A&AS*, 117, 393  
 Bondi M., et al., 2003, *A&A*, 403, 857  
 Bower R. G., Benson A. J., Malbon R., Helly J. C., Frenk C. S., Baugh C. M., Cole S., Lacey C. G., 2006, *MNRAS*, in press

Brinkmann W., Laurent-Muehleisen S. A., Voges W., Siebert J., Becker R. H., Brotherton M. S., White R. L., Gregg M. D., 2000, *A&A*, 356, 445  
 Canosa C. M., Worrall D. M., Hardcastle M. J., Birkinshaw M., 1999, *MNRAS*, 310, 3  
 Ciliegi P., et al., 1999, *MNRAS*, 302, 222  
 Ciliegi P., et al., 2005, *A&A*, 441, 879  
 Clewley L., Jarvis M. J., 2004, *MNRAS*, 352, 909  
 Condon J. J., 1984, *ApJ*, 284, 44  
 Condon J. J., 1992, *ARA&A*, 30, 575  
 Condon J. J., 1997, *PASP*, 109, 166  
 Condon J. J., Cotton W. D., Greisen E. W., Yin Q. F., Perley R. A., Taylor G. B., Broderick J. J., 1998, *AJ*, 115, 1693  
 Connolly A. J., Szalay A. S., Dickinson M., Subbarao M. U., Brunner R. J., 1997, *ApJ*, 486, L11  
 Croton D. J., et al., 2006, *MNRAS*, 365, 11  
 de Ruiter H. R., Arp H. C., Willis A. G., 1977, *A&AS*, 28, 211  
 Dunlop J. S., Peacock J. A., 1990, *MNRAS*, 247, 19  
 Eddington A. S., 1913, *MNRAS*, 73, 359  
 Falcke H., Sherwood W., Patnaik A. R., 1996, *ApJ*, 471, 106  
 Fanaroff B. L., Riley J. M., 1974, *MNRAS*, 167, 31P  
 Ferrarese L., Merritt D., 2000, *ApJ*, 539, L9  
 Fioc M., Rocca-Volmerange B., 1997, *A&A*, 326, 950  
 Furusawa H., et al., 2006, in preparation  
 Geach J. E., Simpson C., Rawlings S., Read A., Watson M., 2006, in preparation  
 Gebhardt K., et al., 2000, *ApJ*, 543, L5  
 Gruppioni C., Mignoli M., Zamorani G., 1999, *MNRAS*, 304, 199  
 Gruppioni C., Zamorani G., de Ruiter H. R., Parma P., Mignoli M., Lari C., 1997, *MNRAS*, 286, 470  
 Gruppioni C., et al., 1999, *MNRAS*, 305, 297  
 Hardcastle M. J., Worrall D. M., 2000, *MNRAS*, 314, 359  
 Hopkins A. M., Afonso J., Chan B., Cram L. E., Georgakakis A., Mobasher B., 2003, *AJ*, 125, 465  
 Ivison R. J., et al., 2006, in preparation  
 Jarvis M. J., Rawlings S., 2004, *NewAR*, 48, 1173  
 Katgert P., Oort M. J. A., Windhorst R. A., 1988, *A&A*, 195, 21  
 Kellermann K. I., Sramek R., Schmidt M., Sahffer D. B., Green R. 1989, *AJ*, 98, 1195  
 Kroupa P., 2001, *MNRAS*, 322, 231  
 Lawrence A., et al., 2006, *MNRAS*, submitted (astro-ph/0604426)  
 Mortier A. M. J., et al., 2005, *MNRAS*, 363, 509  
 Overzier R. A., Röttgering H. J. A., Rengelink R. B., Wilman R. J., 2003, *A&A*, 405, 53  
 Peacock J. A., 1983, *MNRAS*, 202, 615  
 Peacock J. A., Dodds S. J., 1994, *MNRAS*, 267, 1020  
 Prandoni I., Gregorini L., Parma P., de Ruiter H. R., Vettolani G., Wieringa M. H., Ekers R. D., 2001, *A&A*, 365, 392  
 Ranalli P., Comastri A., Setti G., 2003, *A&A*, 399, 39  
 Rawlings S., Saunders R., 1991, *Nature*, 349, 138  
 Reid M. J., Schneps M. H., Moran J. M., Gwinn C. R., Genzel R., Downes D., Rönnäng B., 1988, *ApJ*, 330, 809  
 Richards E. A., 2000, *ApJ*, 533, 611  
 Richards E. A., Kellermann K. I., Fomalont E. B., Windhorst R. A., Partridge R. B., 1998, *AJ*, 116, 1039  
 Risaliti G., Maiolino R., Salvati M., 1999, *ApJ*, 522, 157  
 Sekiguchi K., Takata T., Simpson C., Akiyama, M., 2001, in R. Clowes, A. Adamson, G. Bromage, eds *ASP 232: The New Era of Wide Field Astronomy*, p. 458 (ASP: San Francisco)  
 Sekiguchi K., et al., 2006, in preparation  
 Seymour N., McHardy I. M., Gunn K. F., 2004, *MNRAS*, 352, 131  
 Somerville R. S., Lee K., Ferguson H. C., Gardner J. P., Moustakas L. A., Gialalisco M., 2004, *ApJ*, 600, L171  
 Sullivan M., Hopkins A. M., Afonso J., Georgakakis A., Chan B., Cram L. E., Mobasher B., Almeida C., 2004, *ApJS*, 155, 1  
 Sutherland W., Saunders W., 1992, *MNRAS*, 259, 413  
 Ueda Y., Akiyama M., Ohta K., Miyaji T., 2003, *ApJ*, 598, 886  
 Ueda Y., et al., 2006, in preparation  
 Vanden Berk D. E., et al., 2001, *AJ*, 122, 549

- Waddington I., Dunlop J. S., Peacock J. A., Windhorst R. A., 2001, MNRAS, 328, 882
- White R. L., Becker R. H., Helfand D. J., Gregg M. D., 1997, ApJ, 475, 479
- Willott C. J., Rawlings S., Blundell K. M., Lacy M., Hill G. J., Scott S. E., 2002, MNRAS, 335, 1120
- Willott C. J., Rawlings S., Jarvis M. J., Blundell K. M., 2003, MNRAS, 339, 173
- Windhorst R. A., Fomalont E. B., Partridge R. B., Lowenthal J. D., 1993, ApJ, 405, 498
- Windhorst R., Mathis D., Neuschaefer L., 1990, in ASP 10: Evolution of the Universe of Galaxies, ed. R. G. Kron, p. 389 (ASP: San Francisco)
- Windhorst R. A., Miley G. K., Owen F. N., Kron R. G., Koo D. C., 1985, ApJ, 289, 494
- Windhorst R. A., van Heerde G. M., Katgert P., 1984, A&AS, 58, 1
- Wolstencroft R. D., Savage A., Clowes R. G., MacGillivray H. T., Leggett S. K., Kalafi M., 1986, MNRAS, 223, 279

## APPENDIX A: EXTENDED SOURCES

In this Appendix, we present radio/optical overlays of radio sources with significantly extended morphologies (Fig. A1), together with our assessments of the proposed optical counterparts (see Section 4.1). We also provide brief notes on each source. All spectroscopic redshifts quoted are from M. Akiyama (private communication) unless otherwise noted. Colours are measured in 2-arcsec diameter apertures (Furusawa et al. 2006).

- (a) VLA0001 (J021827–04546) is the brightest source in our catalogue. It is an edge-darkened source *reliably* identified with a large elliptical galaxy.
- (b) VLA0003 (J021839–04418) is a small ( $D = 7.5''$ ) double radio source *reliably* identified with an extended blue object at its centre.
- (c) VLA0007 (J021659–04493) is a giant radio source ( $D = 129''$ ). Although no radio core is seen ( $S_{1.4} < 46 \mu\text{Jy}$ ), there is only one plausible optical ID, a very red galaxy ( $R - z' = 2.0$ ) almost exactly midway between the radio hotspots, and we consider this a *reliable* identification.
- (d) VLA0011 (J021823–05250) is a wide-angle radio source, whose bright core ( $S_{1.4} = 3930 \pm 30 \mu\text{Jy}$ ) is coincident with a large red galaxy. Such sources typically reside in galaxy clusters, and the surrounding objects display a clear red sequence (Geach et al., in preparation) but there is no X-ray emission (Y. Ueda, private communication).
- (e) VLA0012 (J021634–04550) is a large ( $D = 144''$ ) FR II source, whose bright radio core ( $S_{1.4} = 992 \pm 16 \mu\text{Jy}$ ) is coincident with a red galaxy.
- (f) VLA0015 (J021932–05075) is a ‘double-double’ radio source with a pronounced change in position angle between the inner and outer lobes. There is no clear core, but there is a very bright ( $R \approx 19$ ) galaxy located between the two inner lobes, which we *reliably* propose as the identification.
- (g) VLA0016 (J021826–04597) is an apparently highly asymmetric (in terms of arm length) triple. A possible optical counterpart is seen near the central (core?) component, but an X-ray source is detected whose position better matches the galaxy between the central and western components. Spectroscopy of this object reveals strong [O II] at  $z = 1.132$ , so it is considered to be a *probable* identification, while the object closest to the central radio component is considered to be *plausible*. A spectrum of this source is desired to see if it displays the characteristic signatures of an active galaxy.
- (h) VLA0017 (J021827–05348) has no likely optical ID at the location of the radio source peak, but a blue unresolved source is seen

in the southwestern extension. An optical spectrum of this reveals it to be a  $z = 2.579$  QSO, and we therefore consider its identification as the optical counterpart to be *certain*, with the radio emission being dominated by a Doppler-boosted jet. This interpretation is further supported by the presence of faint radio emission on the opposite (receding) side of the source.

- (i) VLA0018 (J021724–05128) is a giant source ( $D = 105''$ ) with a well-detected core ( $S_{1.4} = 253 \pm 16 \mu\text{Jy}$ ). It is identified with a red galaxy at  $z = 0.918$ .
- (j) VLA0019 (J021757–05279) has an unusual radio morphology. The only *probable* ID lies between the northernmost two radio peaks, which is a red galaxy at  $z = 0.694$ .
- (k) VLA0020 (J021800–04499) is comprised of two main radio components: a point-like source to the south, and an extended arc-like component. There is also evidence for faint radio emission connecting the southern source to the northern end of the extended component. No optical object is visible at the location of the southern radio peak, but a faint ( $R > 26$ ) red ( $(R - K)_{\text{AB}} \approx 3.5$ ; T. Takata, private communication) object is visible between the two radio components, and we consider this to be a *plausible* identification.
- (l) VLA0024 (J021906–04590) is an edge-darkened source with a strong core ( $S_{1.4} = 868 \pm 16 \mu\text{Jy}$ ) and two jets of radio emission. It is identified with an isolated bright elliptical galaxy.
- (m) VLA0026 (J021856–05283) is associated with an elliptical galaxy at  $z = 0.450$  which is the eastern member of a pair of bright elliptical galaxies apparently at the centre of a cluster. We have investigated the possibility of the radio flux being enhanced by emission from the western galaxy by fitting two Gaussians to the radio map. The fitted components have flux densities of  $1.41 \pm 0.02 \text{ mJy}$  (eastern) and  $1.22 \pm 0.02 \text{ mJy}$  (western), but the western component is displaced by more than 2 arcsec from the optical location of the galaxy, and there is a  $\ll 1$  per cent probability of the western galaxy being the correct identification for a source at this location. We therefore conclude that this is a single radio source.
- (n) VLA0032 (J021926–05155) is a double radio source ( $D = 20''$ ) *reliably* associated with a red ( $R - z' = 2.0$ ) galaxy.
- (o) VLA0033 (J021737–05134) appears to be a core-jet radio source whose proposed optical ID is a red galaxy  $\sim 1''$  away from the radio peak. This galaxy lies at  $z = 0.647$  and is part of a cluster (Geach et al. 2006) and we consider it to be a *reliable* identification based on the radio morphology. The source appears to be strongly lensing a blue object, but the lack of any contaminating emission lines from this sources suggests that the background object is unlikely to be the ID.
- (p) VLA0049 (J021909–05252) is an unresolved radio source coincident with a tadpole-like galaxy. It is included here because the position of the galaxy in the optical catalogue is somewhat displaced from its nucleus (which is coincident with the radio position; see figure) and hence the galaxy has a low formal probability of being the correct identification. However, there can be no doubt that the disturbed galaxy is the optical counterpart and we consider it *certain*.
- (q) VLA0067 (J021834–04580) is either a core-jet source, or possibly a very asymmetric double (the northern peak has a flux density more than 5 times that of the southern peak). If the brighter peak is associated with the core, then the  $R \approx 22$  galaxy indicated has a formal probability of 4.5% of being the correct identification.
- (r) VLA0086 (J021944–05081) is a triple radio source of angular extent  $8''$ . The nature of this source is ambiguous since there are optical counterparts at the locations of both the central and northern radio peaks. However, a chance alignment of three radio sources

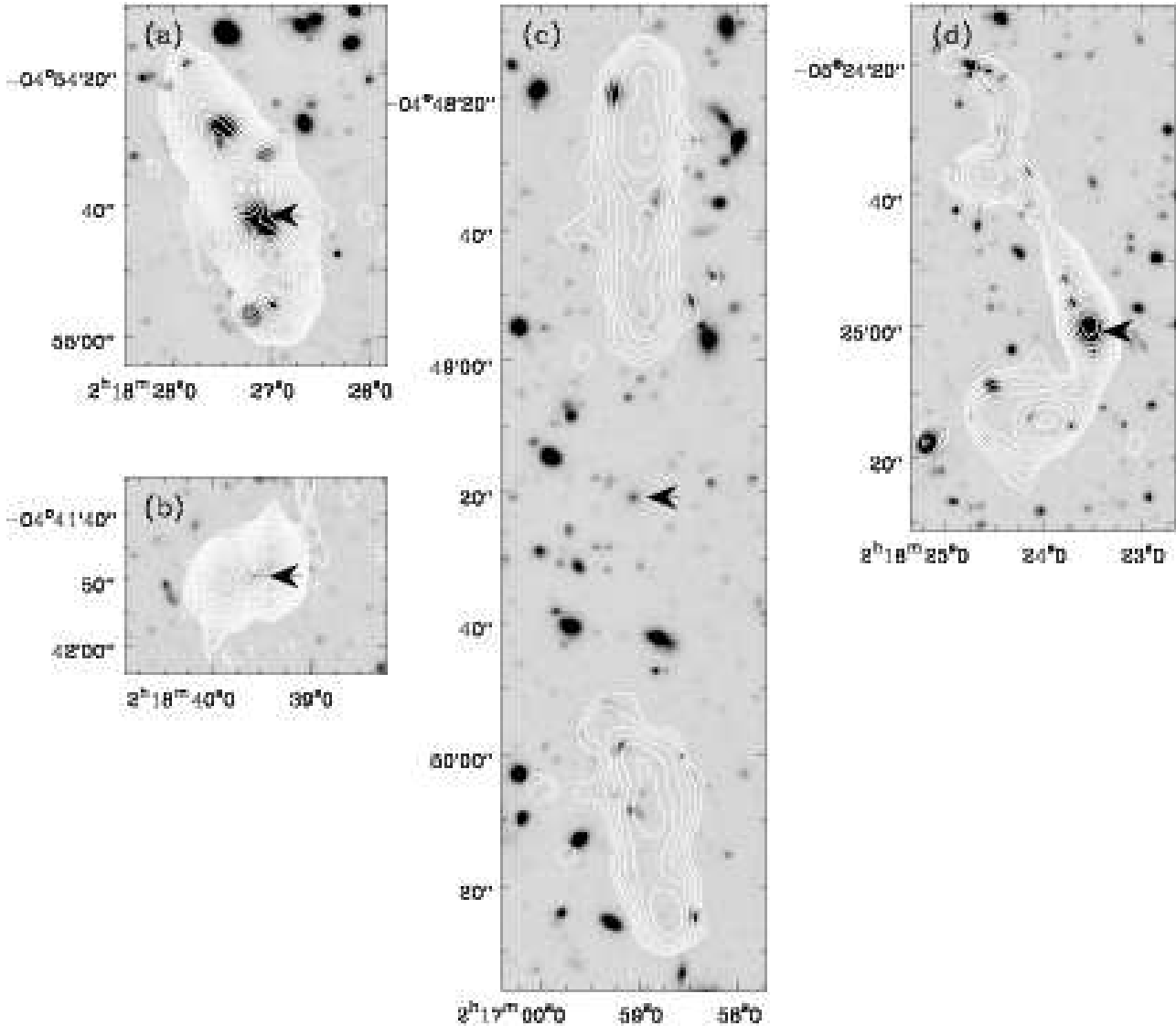


**Figure A1.** Radio/optical overlays of extended radio sources in the SXDF. Radio contours start at  $50 \mu\text{Jy beam}^{-1}$  and are spaced at intervals of  $\sqrt{2}$ . The greyscale is the Subaru/Suprime-Cam  $i'$ -band image, and the proposed identification in each case is marked with an arrow. All images are presented at the same scale. (a) VLA 0001 (J021827–04546) (b) VLA 0003 (J021839–04418) (c) VLA 0007 (J021659–04493) (d) VLA 0011 (J021823–05250).

is improbable, we believe that all three components form a single source, and can provide a formal probability for an identification based on the radio position of the  $R \approx 23$  central source, which is 99.97%. The  $R \approx 20$  galaxy coincident with the northern radio source may contribute to its radio flux.

(s) This is a montage of several distinct radio sources. The brightest (VLA0103 = J021740–4519) is a coreless double *reliably* identified with a 25th magnitude galaxy at its centre. To the north are three radio sources (VLA0167 = J021740–04515; VLA0177 = J021740–04516; VLA0260 = J021740–04517), each coincident with a relatively bright ( $i' \approx 19$ –21) galaxy which have high formal probabilities of being the correct identifications.

(t) VLA0175 (J021808–05222) also cannot be uniquely identified, as there are optical sources coincident with both radio components, as well as midway between them. Given the very similar flux densities of the two components, we consider it most likely to be a double radio source and therefore propose the central galaxy as a *probable* identification.

(u) VLA0244 (J021916–05007) appears to be a double radio source, although there is an additional extension to the southwest of the southern peak. The optical ID is highly uncertain, but we consider the 25th magnitude galaxy between the two main peaks to be a *plausible* identification.

(v) VLA0247 (J021845–05081) is an extended radio source coincident with two galaxies. The peak of the radio emission indicates that the southern galaxy is the identification, but the northern galaxy may contribute some radio flux.

(w) VLA0278 (J021625–05044) possesses extended emission to the east of the radio peak. A 24th magnitude object lies within the eastern extension of the radio source, and this is considered to be a *plausible* identification as the position of the radio peak may not be indicative of the location of the source.

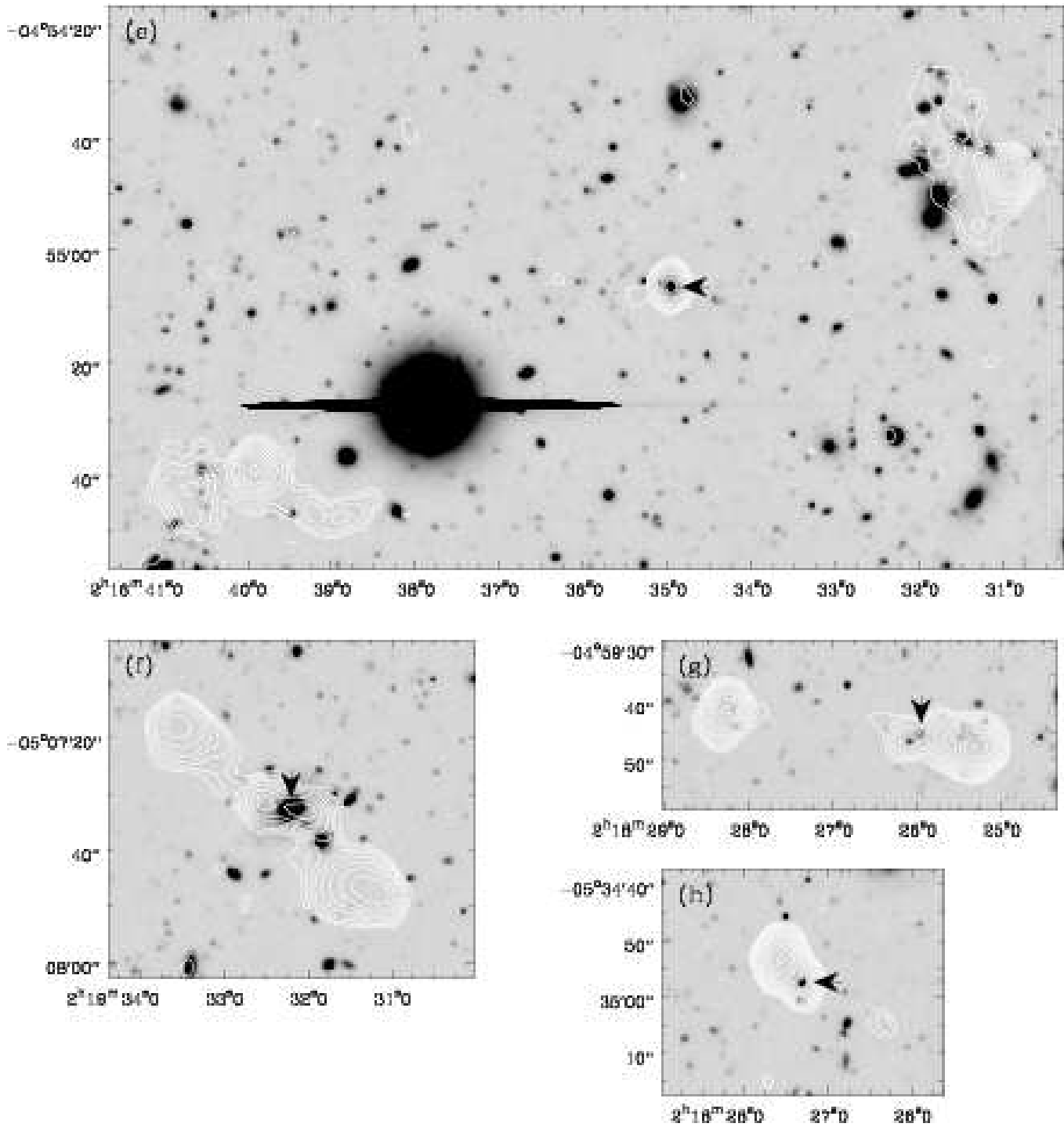


Figure A1. *continued.* (e) VLA 0012 (J021634–04550) (f) VLA 0015 (J021932–05075) (g) VLA 0016 (J021826–04597) (h) VLA 0017 (J021827–050348).



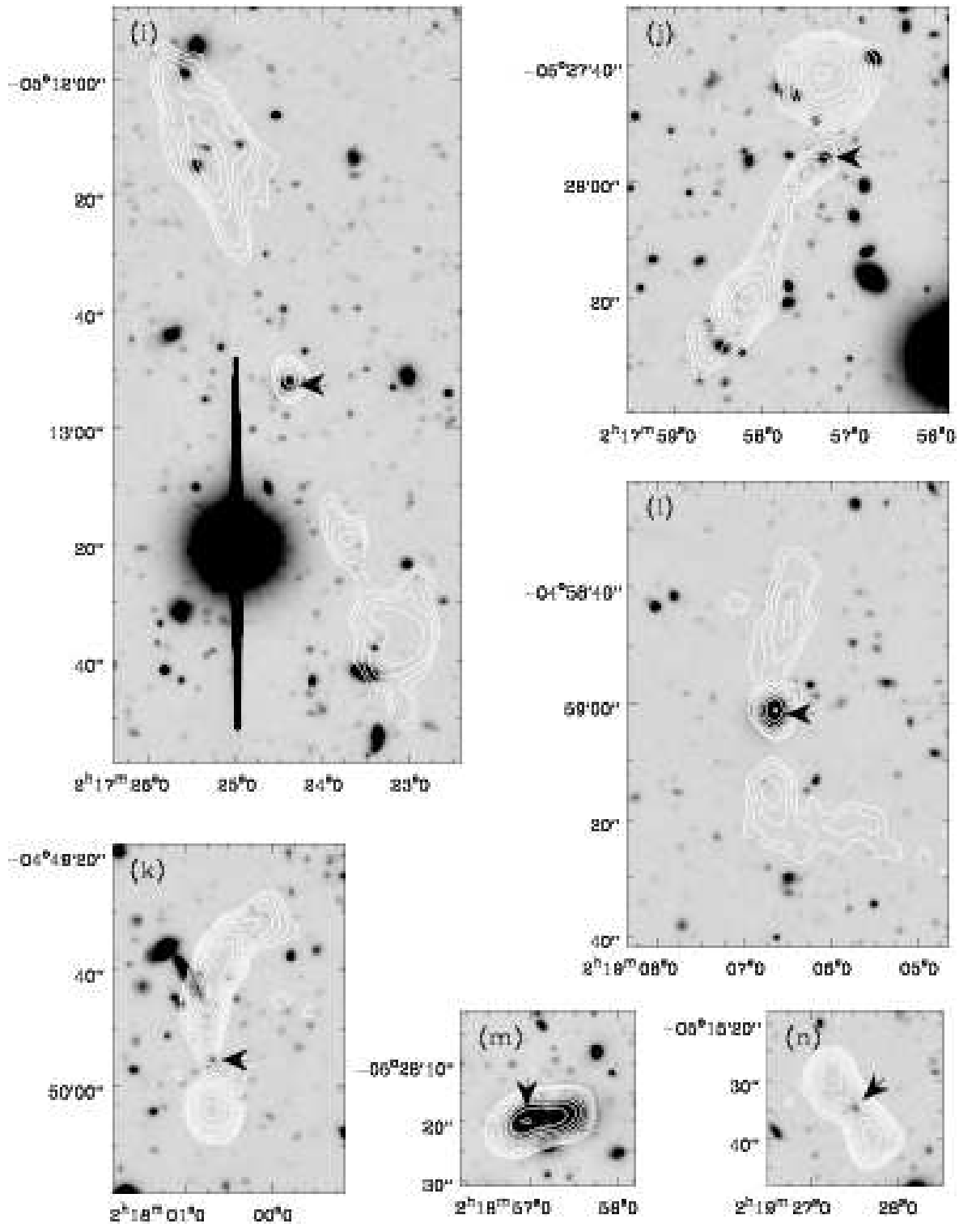
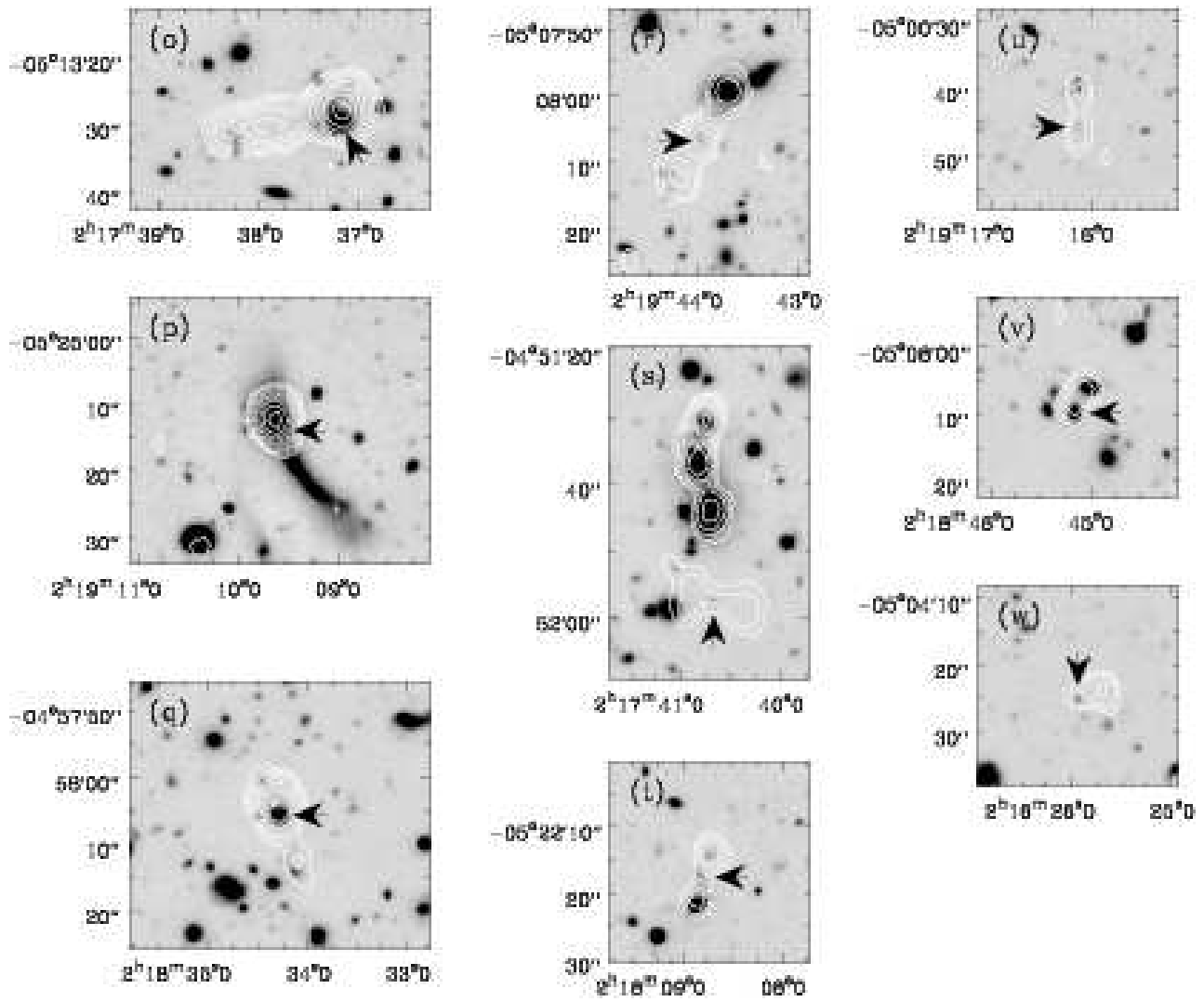


Figure A1. continued. (i) VLA 0018 (J021724–05128) (j) VLA 0019 (J021757–05279) (k) VLA 0020 (J021800–04499) (l) VLA 0024 (J021906–04590) (m) VLA 0026 (J021856–05283) (n) VLA 0032 (J021926–05155).



**Figure A1.** *continued.* (o) VLA 0033 (J021737–05134) (p) VLA 0049 (J021909–05252) (q) VLA 0067 (J021834–04580) (r) VLA 0086 (J021944–05081) (s) VLA 0103 (J021740–04519), VLA 0167 (J021740–04515), VLA 0177 (J021740–04516), and VLA 0260 (J021740–04517) (t) VLA 0175 (J021808–05222) (u) VLA 0244 (J021916–05007) (v) VLA 0247 (J021845–05081) (w) VLA 0278 (J021625–05044).